University of Glasgow
DEPARTMENT OF
AEROSPACE
ENGINEERING

Simulation of Compressible Inviscid Flow on Adaptive Remeshing Unstructured Meshes

Y.F.Yao

Simulation of Compressible Inviscid Flow on Adaptive Remeshing Unstructured Meshes

Y.F.Yao

Dept. of Aerospace Engineering
Aero. Report 9424
University of Glasgow

November 15 ,1994

Simulation of Compressible Inviscid Flow on Adaptive Remeshing Unstructured Meshes

Y.F.Yao
Dept. of Aerospace Engineering
University of Glasgow

Abstracts

An upwinding flux difference splitting method has been used to solve the Euler equations for compressible, inviscid flow on adaptive remeshing unstructured meshes. The method is a cell-centered, finite volume scheme with a Point-Gauss-Seidel (PGS) implicit time-stepping procedure. The high-order resolution has been achieved both by linear reconstruction of the variables and MUSCL approach. The advancing front technique (AFT) has been used to generate the unstructured mesh. The adaptive remeshing procedures based on a series of successive analysis of flow has been used to improve the quality of simulation. The mesh adaptation is accomplished by regeneration using information provided by the computed solution on the current mesh. The approach is demonstracted for four flow field simulations, namely transonic flow over two airfoils and hypersonic flow over a cylinder and blunt body.

Keywords: inviscid flow, unstructured mesh, adaptive remeshing.

1. Introduction

Computational fluid dynamics has now progressed to a stage where the simulation of compressible, inviscid flow modelled by the Euler equation, is commonplace. Normally such simulation includes two main steps. The first is the discretization of the flow domain into a grid which consists of elements(cells) and nodes. The second is then the solution of the governing flow equation ,ie. Euler equation, by numerical approximation methods.

Different approaches to grid generation have been adopted. The most widely used one is the structured mesh [1][2]. Although the structured mesh has its advantages of the simplisity of implementating CFD algorithms on conventional computers and that highly efficient solution techniques such as alternating direction implicit (ADI) iteration schemes or multigrid schemes are permitted, it still meets problems in its capability of generating general complex geometries, currently of interest. On the other hand the unstructured grids, which have been traditionally used with the finite element method, offer a promising

alternative technique for treating such general geometries. Compared to structured meshes, unstructured grids are more flexible to use with complicated geometries and have been shown to be highly effective for mesh adaptivity. The advancing front technique [3] and the Delaunay triangulation [4] are two widely used approaches to generate unstructured grids.

There are many numerical algorithms developed to solve the Euler equations. One approach which has proved popular is the upwinding approach. The strength of upwinding is its capacity of treating the discontinuities in the flow field (such as shock wave regions) and its ability to simulate directly the physics of the directional propagation of information. The most commonly used methods are the flux-difference splitting of Roe [5] and Osher [6] and flux vector splitting of Steger-Warming [7] and Van Leer [8]. These techniques , traditionally used on structured grids, have been successfully applied on unstructured grids recently [9][10].

Compressible flow often includes the narrow regions of high gradients embedded in large areas in which the flow variables vary slowly. As the location of these high gradient regions is not known to the analyst a priori, it is apparent that adaptive remeshing methods, with a posteriori error estimators, will have an important role to play in the development of efficient solutions technique for such flow problems.

Based on our initial researches on supersonic flow [11], this paper presents some interesting results on hypersonic flow and transonic flow problems using an upwinding flux-difference splitting method to solve the Euler equation on adaptive remeshing unstructured grids. The method is a cell-centered, finite volume scheme with a Point-Gauss-Seidel (PGS) implicit time-stepping procedures. The high-order resolution has been achieved both by linear reconstruction of the variables and the variable extrapolation MUSCL approaches. The unstructured grid is generated by using the advancing front technique (AFT) method. The adaptive remeshing procedure, which is based on a series of successive analyses of flow , has been used to improve the quality of flow simulation. These approaches are demonstrated for two hypersonic flows, namely cylinder flow and blunt body flow, and two transonic airfoil flows. The results show the efficiency and robustness of the above method.

2. Governing equations and discretization

2.1 Euler Equations in 2-D

The Euler equations in a Cartesian system of two spatial coordinates in conservation form can be expressed as:

$$\frac{\partial U}{\partial t}+\frac{\partial F_1}{\partial x}+\frac{\partial F_2}{\partial y}=0 \tag{2.1}$$

The expressions for the unknowns and fluxes are

$$U=\begin{pmatrix}\rho\\ \rho u\\ \rho v\\ \rho\varepsilon\end{pmatrix} \qquad F_1=\begin{pmatrix}\rho u\\ \rho u^2+P\\ \rho uv\\ u(\rho\varepsilon+P)\end{pmatrix} \qquad F_2=\begin{pmatrix}\rho v\\ \rho vu\\ \rho v^2+P\\ v(\rho\varepsilon+P)\end{pmatrix} \tag{2.2}$$

where ρ,u,v,P and ε are the density, velocity components in Cartesian coordinates, pressure and specific total energy of the flow, respectively.

2.2 Solution algorithms

The solution algorithm employed in the present paper is an implementation of the Finite-Volume method on unstructured grids. The solution domain Ω is discretized by an assembly of triangular elements. Over a single element Ωe, the integral form of (2.1) is

$$\begin{aligned}\int_{\Omega_e}\frac{\partial U}{\partial t}d\Omega &= \int_{\Omega_e}\left(-\frac{\partial F_1}{\partial x}-\frac{\partial F_2}{\partial y}\right)d\Omega\\ &= \int_{\Gamma_e}-n_iF_i d\Gamma \qquad\qquad i=1,2\end{aligned} \tag{2.3}$$

Where: $n_i=(n_1,n_2)$ denotes the unit vector outward normal to the boundary Γe of control volume Ωe.

Assuming a piecewise constant distribution of the unknowns Ue on each element Ωe, Eq(2.3) may be approximated in the form as

$$\Delta U_e=U_e^{n+1}-U_e^n=\frac{\Delta t_e}{\Omega_e}F^I \tag{2.4}$$

Where: U_e^n denotes the valus of Ue at time $t = t^n$, $\Delta t = t^{n+1} - t^n$ is the time step between t^{n+1} and t^n, F^I denotes the inviscid contributions .

The inviscid contributions F^I are given by

$$F^I = \int_{\Gamma_e} -n_i F_i d\Gamma = -\int_{\Gamma_e} F_n d\Gamma \tag{2.5}$$

and can be evaluated by summing the contributions from each individual element side Γes in turn. In this evaluation the normal flux Fn is replaced by a numerical flux $\tilde{F}_n$, so that

$$F^I = -\sum_{Se} \int_{\Gamma_{es}} \tilde{F}_n d\Gamma \tag{2.6}$$

.i.;For a typical side Γ_{es} with associated elements e and r , Roe's linearization is used to construct the matrix A_{roe}, such that

$$F_{nr} - F_{ne} = A_{roe}(U_r - U_e) \tag{2.7}$$

and the numerical flux is then taken to be

$$\tilde{F}_n = 0.5[F_{ne} + F_{nr} - |A_{roe}|(U_r - U_e)] \tag{2.8}$$

Here it has been assumed that A_{roe} has been factored as

$$A_{roe} = R^{-1}\Lambda R \tag{2.9}$$

where Λ is a diagonal matrix containing the eigenvalues λ_i of A_{roe} and $|A_{roe}|$ is defined by

$$|A_{roe}| = R^{-1}|\Lambda|R \tag{2. 10 }$$

Details about the formula can be found in Ref.[12] and [13].

The mininum allowable value for λ_i is restricted according to the method proposed by Harten [14] and is such that:

$$|\lambda_i| = \begin{cases} |\lambda_i| & |\lambda_i| > \varepsilon_\lambda \\ 0.5(\lambda_i^2 / \varepsilon_\lambda + \varepsilon_\lambda) & |\lambda_i| \le \varepsilon_\lambda \end{cases} \tag{2.11}$$

where ε_λ is the eigenvalue limiter.

2.3 Point-Gauss-Seidel Implcit Schemes

If the inviscid contributions are evaluated at time t^{n+1}, equation (2.4) leads to the implicit scheme

$$\Delta U_e = -\frac{\Delta t_e}{\Omega_e} \sum_{S_e} \left\{ \frac{1}{2}\left[F_e^{n+1} + F_r^{n+1} - |A_{Roe}^{n+1}|(U_r^{n+1} - U_e^{n+1}) \right] \right\} \delta s_e \tag{2.12}$$

Linearization of this equation for the values of the unknowns and fluxs result in

$$\left[I + \frac{\Delta t_e}{2\Omega_e} \sum_{S_e} \left| A^*_{Roe} \right| \delta s_e \right] \Delta U_e^{n+1} = -\frac{\Delta t_e}{2\Omega_e} \sum_{S_e} \left[F_e^n + F_r^* - \left| A^*_{Roe} \right| \left(U_r^* - U_e^n \right) \right] \delta s_e \tag{2.13}$$

where the linearization has been performed with all iterative solution in mind and the terms denoted by an asterisk are evaluted using the latest available solution in the adjacent elements. Thus the iterative procedure may be regarded as a point-Gauss-Seidel method requiring the inversion of a 4*4 matrix for each element in the computational grid.

2.4 Boundary Condition

For Euler equations all the boundary conditions used for the exterior boundary are based on the method of characteristics. For the wall boundary, i.e a solid wall, the appropriate boundary conditions are the nonslip wall boundary condition, which means that the normal component of the velocity to the wall is zero.

Using the velocity tangency condition in equations Fn

$$F_n = \begin{pmatrix} \rho U_n \\ \rho u U_n + P n_x \\ \rho v U_n + P n_y \\ U_n(\rho\varepsilon + P) \end{pmatrix} \tag{2.14}$$

i.e U_n=0, then the fluxes at the wall are obtained in the following expression

$$F_W = \begin{pmatrix} 0 \\ P_W n_x \\ P_W n_y \\ 0 \end{pmatrix} \tag{2.15}$$

It is necessary then to determine the pressure at the wall. This also means only the pressure contribution remains at the walls. Various methods can be applied in order to obtain the wall pressure, such as Characteristic Relations and Extrapolation.

For the implicit scheme, however, further care is needed. The Jacobian matrix of the transformation Ue ---> Fw must also be used on the left hand side of the implicit equation system. It is

$$A_W = (\gamma - 1) \begin{pmatrix} 0 & 0 & 0 & 0 \\ \frac{u^2+v^2}{2} n_x & -u n_x & -v n_x & -n_x \\ \frac{u^2+v^2}{2} n_y & -u n_y & -v n_y & -n_y \\ 0 & 0 & 0 & 0 \end{pmatrix} \tag{2.16}$$

As an example the implicit formulation for an element adjacent to the wall using the numerical flux of Roe is explained. Equation (2.13) is now written as

(in form of P-G-S)

$$\left[I + \frac{\Delta t_e}{\Omega_e} [\sum_{Se \neq W} (A_e^n + \left| A_{Roe}^* \right|) \delta s_e + 2 A_W^n \delta_W] \right] \Delta U_e =$$

$$- \frac{\Delta t_e}{\Omega_e} \left(\sum_{Se \neq W} 0.5 * \left[F_e^n + F_r^* - \left| A_{Roe}^* \right| (U_r^* - U_e^n) \right] \delta s_e + F_W^n \delta_W \right) \tag{2.17}$$

2.5 High-Order Resolutions

Here we use two methods to construct high-order resolutions. One is called linear reconstruction of variables proposed by Barth & Jesperson [9]. The other is directly using variable extrapolation (MUSCL) reported by Batina [15]. Details can be found in reference [11].

3. Mesh generation

3.1 Advancing Front Technique (AFT)

The algorithm for the grid generation is the advancing front technique[3]. The generation procedure consists of subdividing an arbitrarily complex domain into a consistant assembly of elements. The consistency of the generated grid is guaranteed if the generated elements cover the entire domain and the intersection between elements occurs only on common points and sides. The final grid is constructed in a bottom-up manner. The process starts by discretising each boundary curve. Nodes are placed on the boundary curve components and then contiguous nodes are joined with straight line segments. In later stages of the generation process, these segments will become sides of some triangles. The length of these segments must therefore, be consistent with the desired local distribution of grid size. This operation is repeated for each boundary curve in turn. The next stage consists of generating triangular planar faces. For each two dimensional region to be discretised, all the edges produced when discretising its boundary courves are assembled into the so called initial front. The relative orientation of the curve components with respect to the surface must be taken into account in order to give the correct orientation to the sides in the initial front. The front is a dynamic data structure which changes continuously during he generation process. At any given time, the front contains the set of all the sides which are currently available to form a triangular face. A side is selected from the front and a triangular element is generated. This may involve creating a new node or simple connecting to an

existing one. After the triangle has been generated, the front is updated and the generation proceeds until the front is empty. The size and shape of the generated triangles must be consistent with the local desired size and shape of the final grid. Such an approach is utilized in present work.

3.2 Adaptive remeshing procedure

Mesh adaption is an important procedure in numerical flow simulation. It offers the prospect of accurate flow field simulations without the use of excessively fine, computationally expensive meshes. In this case small elements are used only in the regions where the flow is complex whereas bigger elements are used in the rest of the domain. A general scheme using this strategy requires three steps. Firstly, an unstructured mesh generator, able to control the sizes of the elements everywhere, is needed. Secondly, the flow solver is used to calculate physical flow variables . Thirdly, an a posteriori error estimator or indicator is required, which reveals where in the flow field the mesh is deficient and requires some smaller elements in these region. Of the many methods avaiable for mesh adaptation [16] the remeshing procedure is fairly easy to implement on unstructured grids and has been coupled with a flow solver.

The following technique is used to locate the high flow gradient regions. The gradient across an edge is computed, for example, as

$$\Delta = \frac{\rho_e - \rho_r}{\rho_e + \rho_r}$$

Here the flow variable ρ, the density, has been chosen as the error indicator. The region including that edge must be replaced by smaller elements if $\Delta \geq A_R$, where A_R is a specified parameter with a value normally between 0.05 and 0.2. After completion we have found the regions which need smaller elements. The flow domain can then be remeshed by changing some control parameter to meet requirementts(such as mesh size).

4. Results

4.1 Hypersonic cylinder flow

The first test case is the hypersonic flow over a sector of a cylinder with a free stream Mach number of 8.0. The coarse mesh used, which contains 1615 elements and 875 nodes,

is generated by the AFT method(see Fig.1). The flow field vector plot is illustrated on Fig.2(a) (full domain) and Fig.2(b) (zoom --- stagnation regions). Figure 3-5 gives the pressure, density and Mach number contours. After using the error indicator we can find there exists a high gradient region in the flow domain. After remeshing we get the fine mesh (see Fig.6) with 2985 elements and 1560 nodes. Smaller elements are mainly located in the high gradient region that is detected. Fig.7 gives the flow field vector plot. Figs 8-10 give the pressure, density and Mach number contours. It can be seen that the quality of simulation is improved after the remeshing procedure. All these computations use high-order (MUSCL) approaches.

4.2 Hypersonic blunt body flow

The second test case is the hypersonic flow over a blunt body with a free stream Mach number of 10.0 and zero incidence angle. The coarse mesh used, which contains 899 elements and 499 nodes, is generated by the AFT method(see Fig.11). The flow field vector plot is illustrated in Fig.12. Figures 13-15 give the pressure, density and Mach number contours. After checking for the gradient value by using error indicator we can find out the high gradient regions . After remeshing we generate the fine mesh (see Fig.16), which contains 2697 elements and 1400 nodes. Many more smaller elements are located in the high gradient region than expected. Fig.17 gives the flow field vector charts. Figs 18-20 give the pressure, density and Mach number contours. Similar to the cylinder flow it can be seen that the quality of simulation is improved after the remeshing procedure. These computations used high-order (MUSCL) approaches.

4.3 NACA 0012 airfoil --- transonic flow

Two test cases considered are the supercritical flow over a NACA 0012 airfoil with (a) a freestream Mach number of 0.75 and an incidence angle of 2.0° and (b) a freestream Mach number of 0.80 and an incidence angle of 1.25°. Mesh 1 shown in Figure 21 is used for the initial guess. This mesh consists of 3246 elements and 1670 nodes. The Mach number and pressure contours for these two test cases are shown in Figure 22-23. The second remeshing grid (Mesh2) can be seen in Figure 24, which contains 6354 elements and 3267 nodes. More smaller elements are set around the surface of the airfoil especially in the leading edge regions. Figure 25-26 shows the contours. In test case (a) we find there remains a high gradient region, ie. shock wave region, after using the error indicator. Smaller elements have been included in that region to capture the shock wave. Figure 27 gives the result of adaptive remeshing grid (Mesh3) in test case (a): which contains 8558 elements and 4381 nodes. Figure 28 provides the results , which is obviously improved especially in the shock

region. All these result are obtained by using first-order schemes. Figure 29 gives the results when using the high-order resolution procedure (linear reconstruction of variables) which are seen to be better than those of first-order. For test case (b) the procedure is nearly the same. Figure 30 shows the adaptive remeshing grid (Mesh3). Figure 31 illustrates the first-order results and figure 36, the high-order results (linear reconstruction of variables). Figure 33 is the comparison of the C_P distribution on different meshes for test case (a). Figure 34 is the comparison of first-order and high-order results for the same mesh,Mesh3, on test case (a). Figure 35 is the comparison of the C_P distribution on different meshes for test case (b). Figure 36 is the comparison of first-order and high-order results on the same mesh, Mesh3, for test case (b).

4.4 RAE 2822 airfoil --- transonic flow

The case considered here is the supercritical flow over a RAE 2822 airfoil with a freestream Mach number of 0.75 and an incidence angle of 3.0°. Mesh 1 shown in Figure 37 is used for the initial guess. This mesh consists of 6674 elements and 3426 nodes. The Mach number and pressure contours for this case are shown in Figure 38. We can also detect that there is a high gradient region after using the error indicator. Smaller elements are again used in that region to capture the smaller changes in that region. Figure 39 gives the result of adaptive remeshing grid (Mesh 2), which contains 9506 elements and 4850 nodes. Figure 40 shows pressure and Mach number contours, which are obviously improved especially in the shock region. All these result are obtained by using first-order schemes. Figure 41 gives the results when using the high-order resolution procedure (linear reconstruction of variables) which are seen to be better than those of first-order. Figure 42 is the comparison of C_P distribution on different meshes. Figure 43 is the comparison of first-order and high-order results on the same mesh (Mesh2) .

5. Conclusions

The cell-centered finite volume scheme with Point-Gauss-Seidel implicit time stepping algorithm has been successfully applied on unstructured grids. The approach has been validated on different geometries and over a range of Mach numbers. High order resolution variants have been implemented. The incorporation of mesh adaptivity, using an adaptive remeshing strategy, substantially improves the quality of the flow simulation.

The experience with above method appears quite promising. However a wider class of flow problems needs to be computed, especially those involving viscous flow. To reach this

target, the construction of the viscous mesh must be considered. Fig.44-46 illustrates an appropraite viscous mesh construction method. We call it the mixing method based on the structured mesh (either O-mesh or C-mesh) and the AFT method.

Acknowledgments

The auther wishes to thank the University of Glasgow for a research scholarship and the CVCP committee for ORS award.

References

[1] J.F.Thompson, Z.U.A.Warsi and C.W. Mastin " Numerical Grid Generation, Foundations and Applications" North-Holland, Amesterdam,1985

[2] N.P. Weathrill and C.R.Forsey " Grid generation anbd flow calculations for aircraft geometries" J.Aircraft ,22,855-860 ,1985

[3] J.Peraire, J.Peiro, L.Formaggia, K.Morgan and O.C.Zienkiewicz, "Finite element Euler compuattion in three dimensions" AIAA paper 88-0032 ,1988

[4] A.Jameson, T.J.Baker and N.P. Weatherill " Calculation of inviscid transonic flow over a complete aircraft" AIAA paper 86-0103, 1986

[5] P.L. Roe " Approximate Riemann solvers,parameter vectors and difference schemes" J.Comput.Phys., 43,357 (1981)

[6] S.Osher "Numerical solution of singular perturbation problems and hyperbolic systems of conservation laws" North-Holland Mathematical Studies, Vol. 97, North-Holland, Amsterdam, 1981, p.179

[7] J.L.Steger and R.F.Warming " Flux vector splitting of the inviscid gasdynamic equations with application to finite diference methods" J.Comput. Phys. 40,263 (1981)

[8] B.Van Leer 'Flux-vector splitting for the Euler equations " Lecture Notes in Physics, Vol.170, Springer, Berlin, 1982 P.507

[9] T.J.Barth and D.C.Jesperson " The design and application of upwinding schemes on unstructured meshes" AIAA paper 89-0366 1989

[10] M.Vahdati, K.Morgan, J.Peraire and O.Hassan " A cell-vertex upwind unstructured grid solution procedure for high speed compressible viscous flow " in Proc. royal AeronauticAl Society Int. Conf. on Hypersonic Aerodynamics, Manchester, 12.1-12.22, 1989

[11] Y.F.Yao " Implicit High-Order Resolution of Supersonic Flow on Unstructured Grids" Dept. of Aerospace Engineering Aero.Report 9409, University of Glasgow

[12] L.Dubuc "Two-Dimensional Navier-Stokes Solver Using An Upwind Scheme on Unstructured Grids" Final Report, Sept.1992 Dept. of Aeorspace Engineering, University of Glasgow

[13] S.Soltani "An Upwind Scheme for the Equations of Compressible Flow on Unstructured Grids" Thesis submitted for the degree of Doctor of philosophy of the University of London, July 1991

[14] A.Harten " High resolution schemes for hypersonic conservation law " DOE/ER/03077-175, Courant Mathematics and Computing Lab. NYU,1982

[15] J.T.Batina "Implicit Flux-Split Euler Schemes for Unsteady Aerodynamic Analysis Involving Unstructured Dynamic Meshes" AIAA J. Vol.29 No.11,1991 pp 1836-1843

[16] N.P. Weathrill " Gird Generation" VKI Lecture Series 1990-10, Brussels,Belgium,June 1990

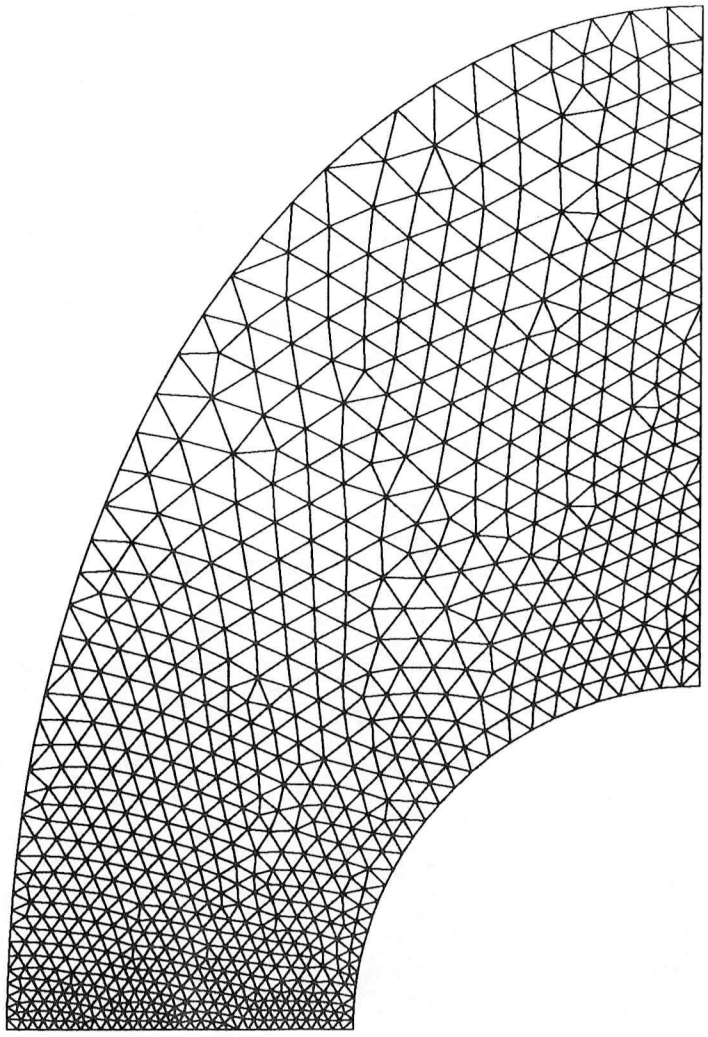

UNSTRUCTURED GRID

Model: Cylinder Flow
Code : Euler Equation
PGS scheme
Flux : Roe
Order : high-order
Mesh : Corse Mesh
1615 elements
875 nodes
133 boundary points
Free stream condition :

$M_{inf} = 8.0$

$T_{inf} = 32.6K$

$T_w = 300K$

Figure 1 Unstructured grid around cylinder body (corse mesh)

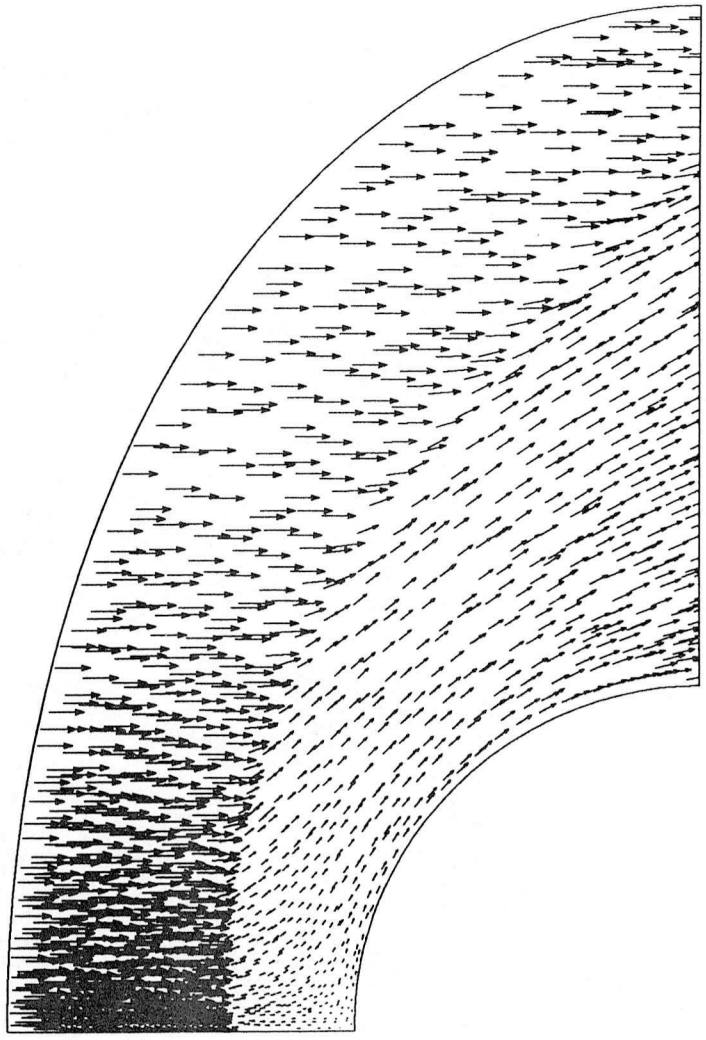

FLOW FIELD

Model: Cylinder Flow
Code : Euler Equation
PGS scheme
Flux : Roe
Order : high-order
Mesh : Corse Mesh
1615 elements
875 nodes
133 boundary points
Free stream condition :

$M_{inf} = 8.0$

$T_{inf} = 32.6K$

$T_w = 300K$

Figure 2(a) Cylinder flow (coarse mesh) -- Velocity field

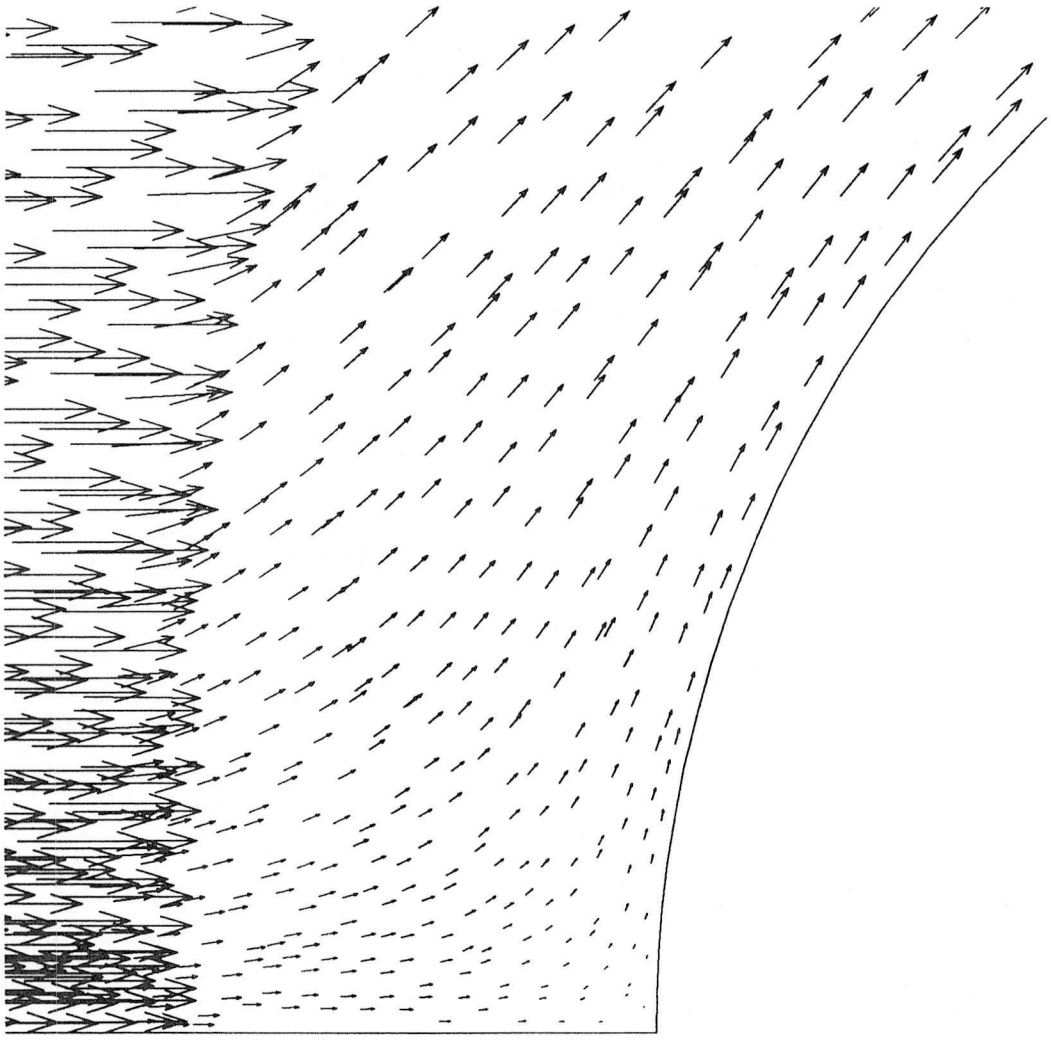

FLOW FIELD

Model: Cylinder Flow
Code : Euler Equation
PGS scheme
Flux : Roe
Order : high-order
Mesh : Coarse Mesh
1615 elements
875 nodes
133 boundary points
Free stream condition :

$M_{inf} = 8.0$

$T_{inf} = 32.6K$

$T_w = 300K$

Figure 2(b) Cylinder flow (coarse mesh) -- Velocity field

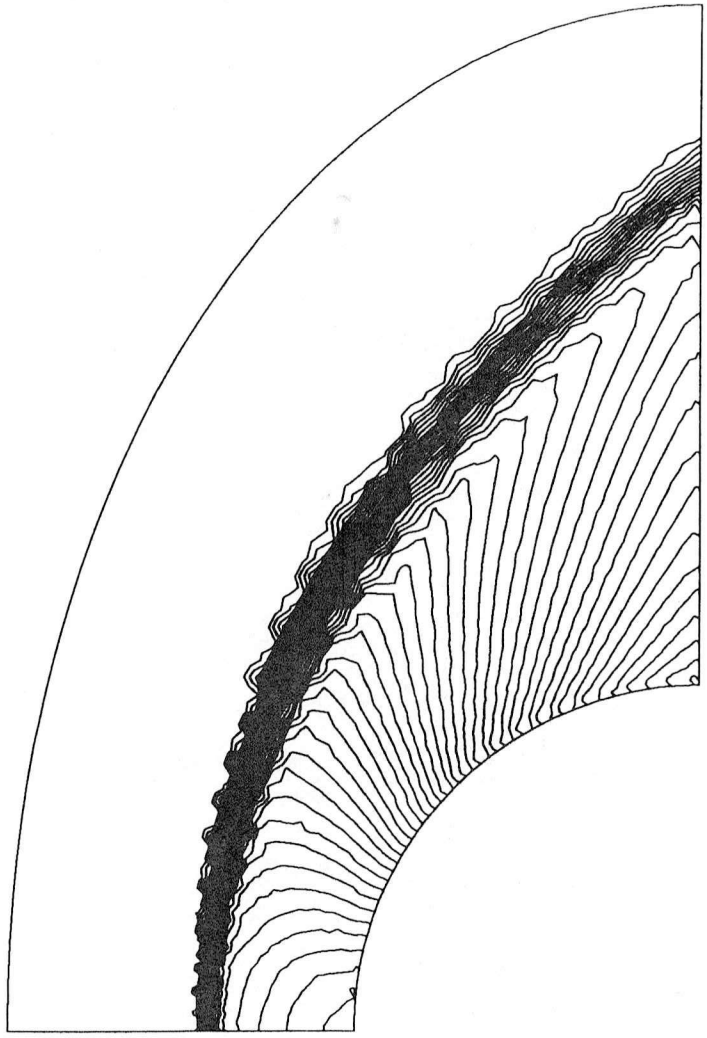

PRESSURE CONTOURS

Model: Cylinder Flow
Code : Euler Equation
PGS scheme
Flux : Roe
Order : high-order
Mesh : Coarse Mesh
1615 elements
875 nodes
133 boundary points
Free stream condition :

$M_{\inf} = 8.0$

$T_{\inf} = 32.6K$

$T_w = 300K$

Figure 3 Cylinder flow (coarse mesh) -- Pressure contours

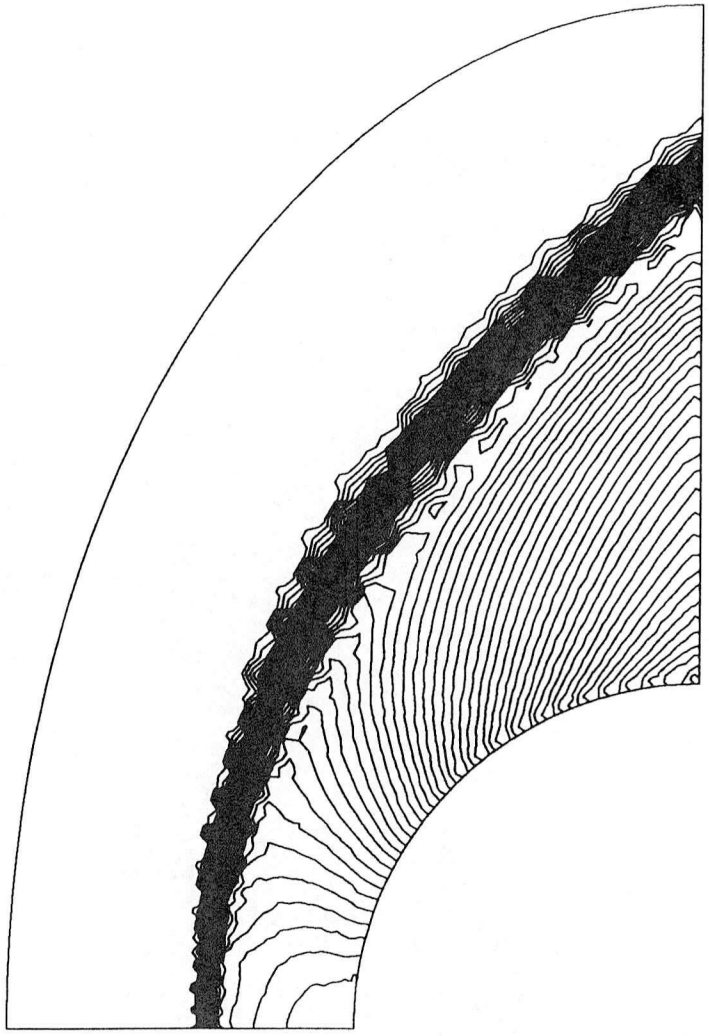

DENSITY CONTOURS

Model: Cylinder Flow
Code : Euler Equation
PGS scheme
Flux : Roe
Order : high-order
Mesh : Coarse Mesh
1615 elements
875 nodes
133 boundary points
Free stream condition :

$M_{inf} = 8.0$

$T_{inf} = 32.6K$

$T_w = 300K$

Figure 4 Cylinder flow (coarse mesh) -- Density contours

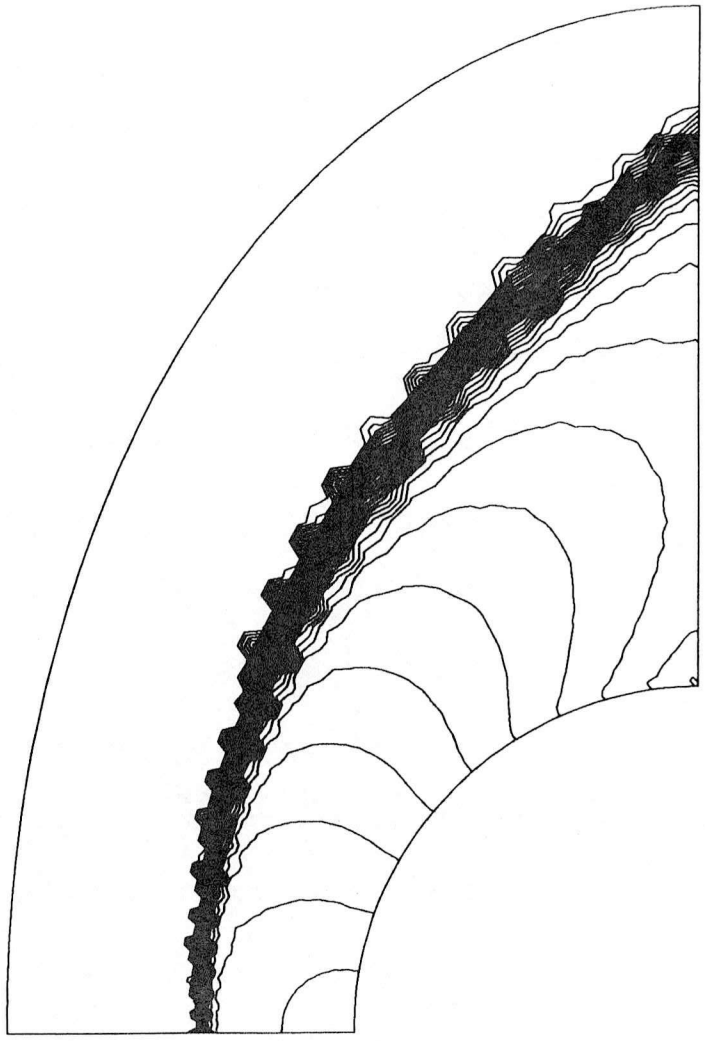

MACH NUMBER CONTOURS

Model: Cylinder Flow
Code : Euler Equation
PGS scheme
Flux : Roe
Order : high-order
Mesh : Coarse Mesh
1615 elements
875 nodes
133 boundary points
Free stream condition :

$M_{inf} = 8.0$

$T_{inf} = 32.6K$

$T_w = 300K$

Figure 5 Cylinder flow (coarse mesh) -- Mach contours

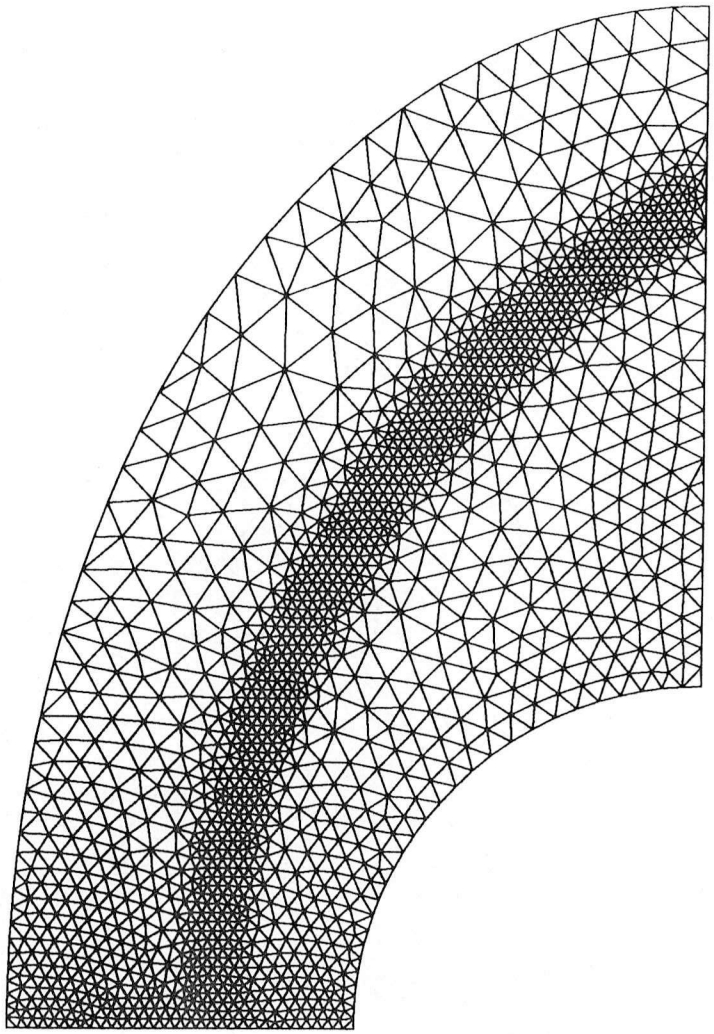

UNSTRUCTURED GRID

Model: Cylinder Flow
Code : Euler Equation
PGS scheme
Flux : Roe
Order : high-order
Mesh : Fine Mesh
2985 elements
1560 nodes
133 boundary points
Free stream condition :

$M_{inf} = 8.0$

$T_{inf} = 32.6K$

$T_w = 300K$

Figure 6 Unstructured grid around cylinder body (fine mesh)

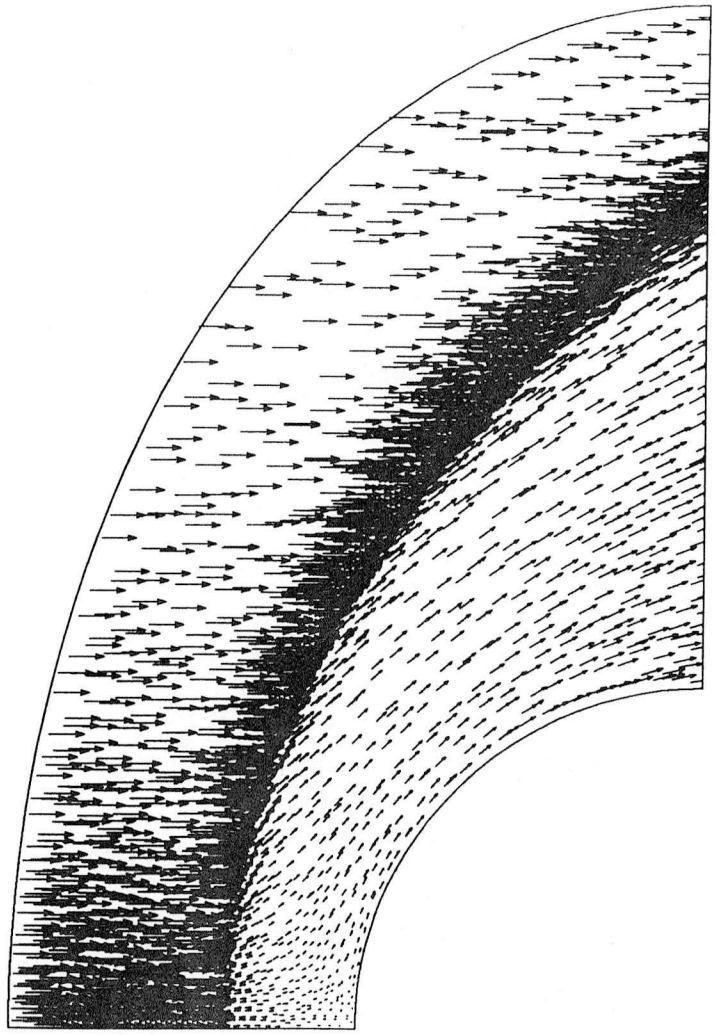

FLOW FIELD

Model: Cylinder Flow
Code : Euler Equation
PGS scheme
Flux : Roe
Order : high-order
Mesh : Fine Mesh
2985 elements
1560 nodes
133 boundary points
Free stream condition :

$M_{inf} = 8.0$

$T_{inf} = 32.6K$

$T_w = 300K$

Figure 7(a) Cylinder flow (fine mesh) -- Velocity field

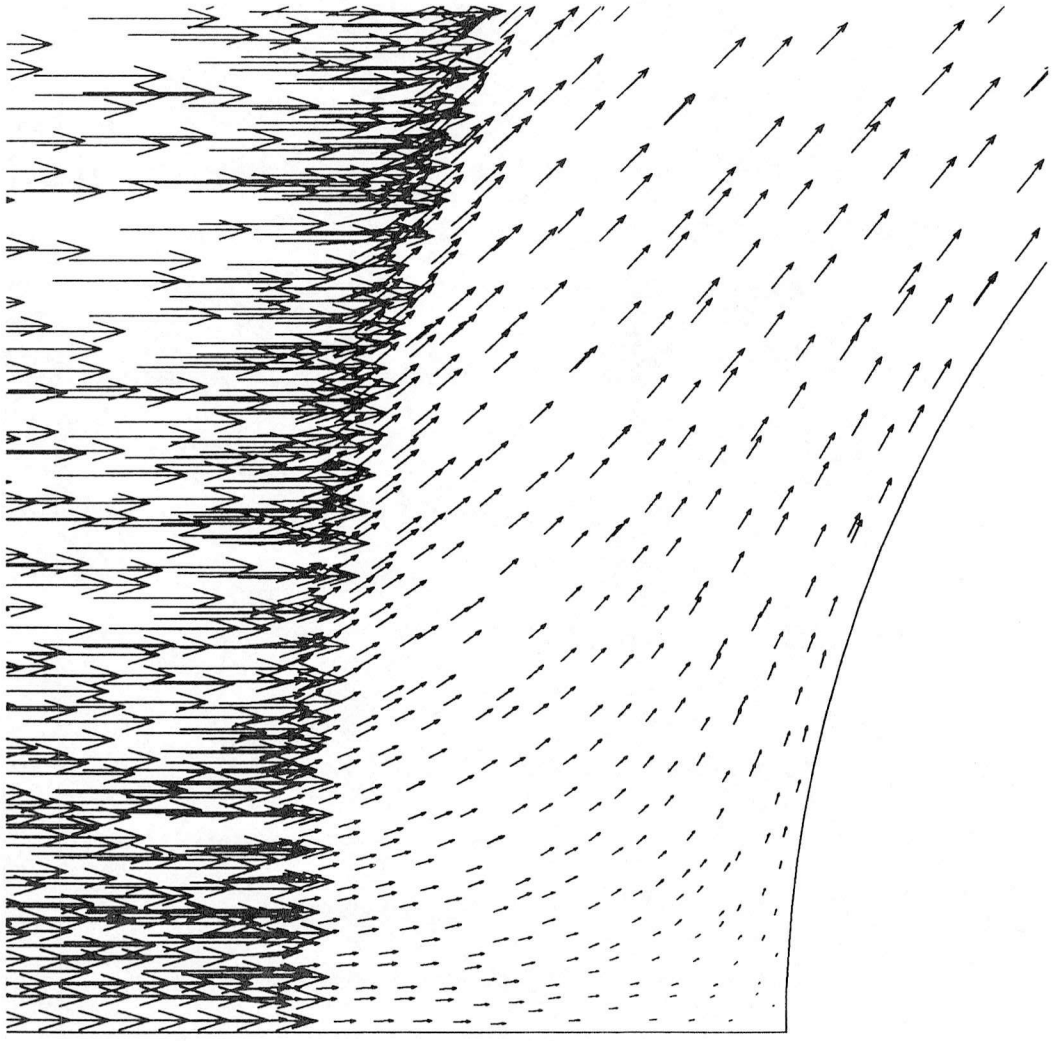

FLOW FIELD

Model: Cylinder Flow
Code : Euler Equation
PGS scheme
Flux : Roe
Order : high-order
Mesh : Fine Mesh
2985 elements
1560 nodes
133 boundary points
Free stream condition :

$M_{inf} = 8.0$

$T_{inf} = 32.6K$

$T_w = 300K$

Figure 7(b) Cylinder flow (fine mesh) -- Velocity field

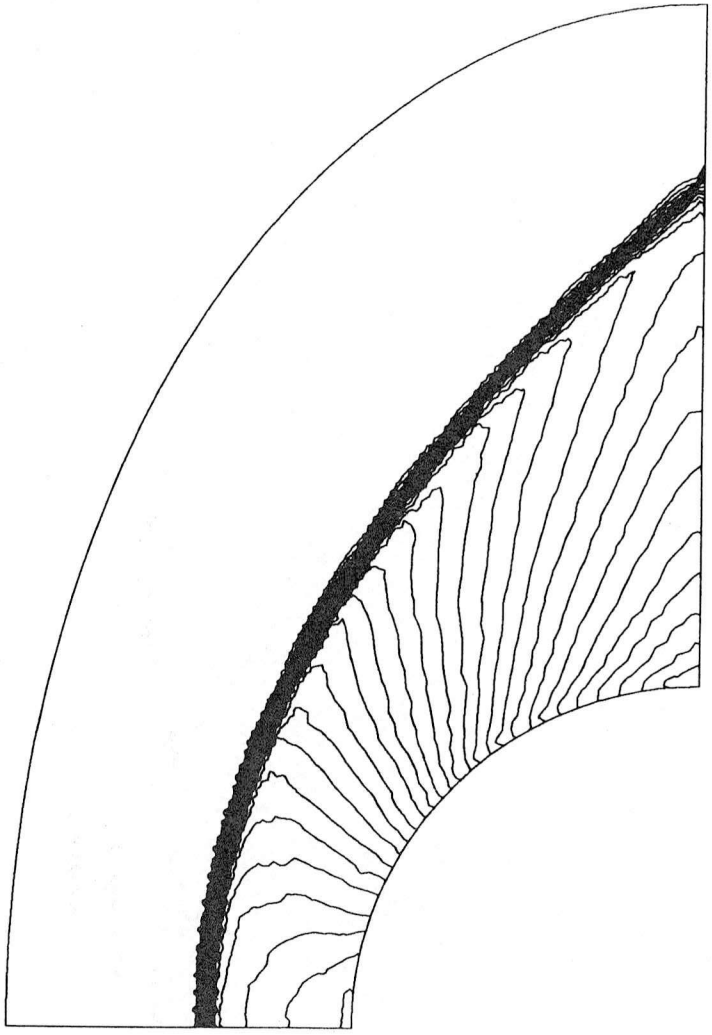

PRESSURE CONTOURS

Model: Cylinder Flow
Code : Euler Equation
PGS scheme
Flux : Roe
Order : high-order
Mesh : Fine Mesh
2985 elements
1560 nodes
133 boundary points
Free stream condition :

$M_{inf} = 8.0$

$T_{inf} = 32.6K$

$T_w = 300K$

Figure 8 Cylinder flow (fine mesh) -- Pressure contours

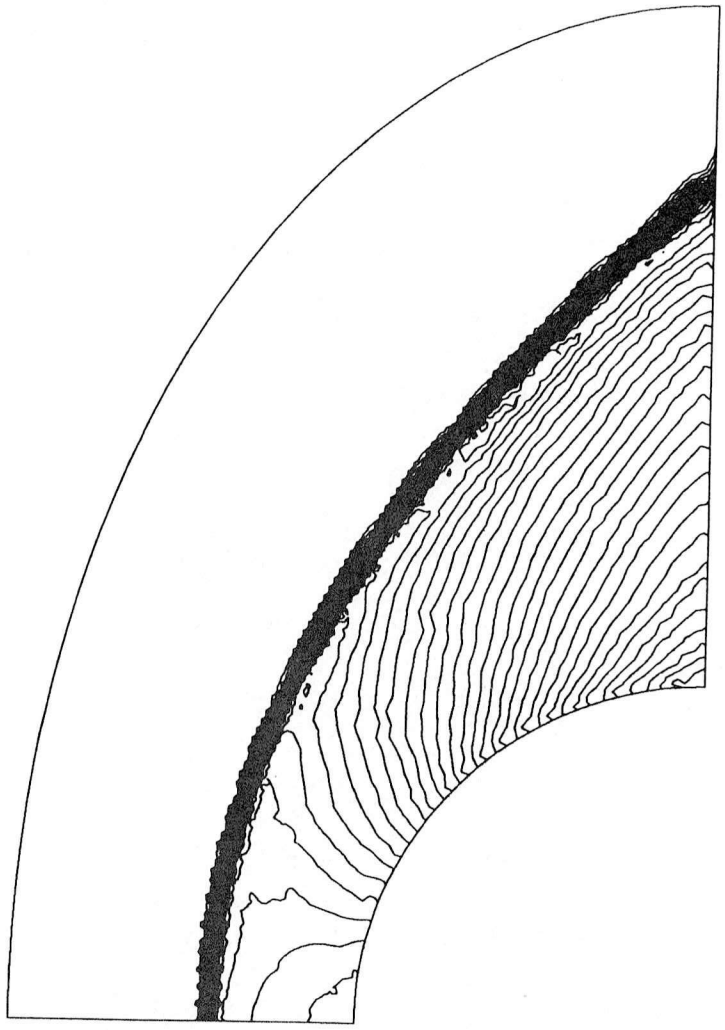

DENSITY CONTOURS

Model: Cylinder Flow
Code : Euler Equation
PGS scheme
Flux : Roe
Order : high-order
Mesh : Fine Mesh
2985 elements
1560 nodes
133 boundary points
Free stream condition :

$M_{inf} = 8.0$

$T_{inf} = 32.6K$

$T_w = 300K$

Figure 9 Cylinder flow (fine mesh) -- Density contours

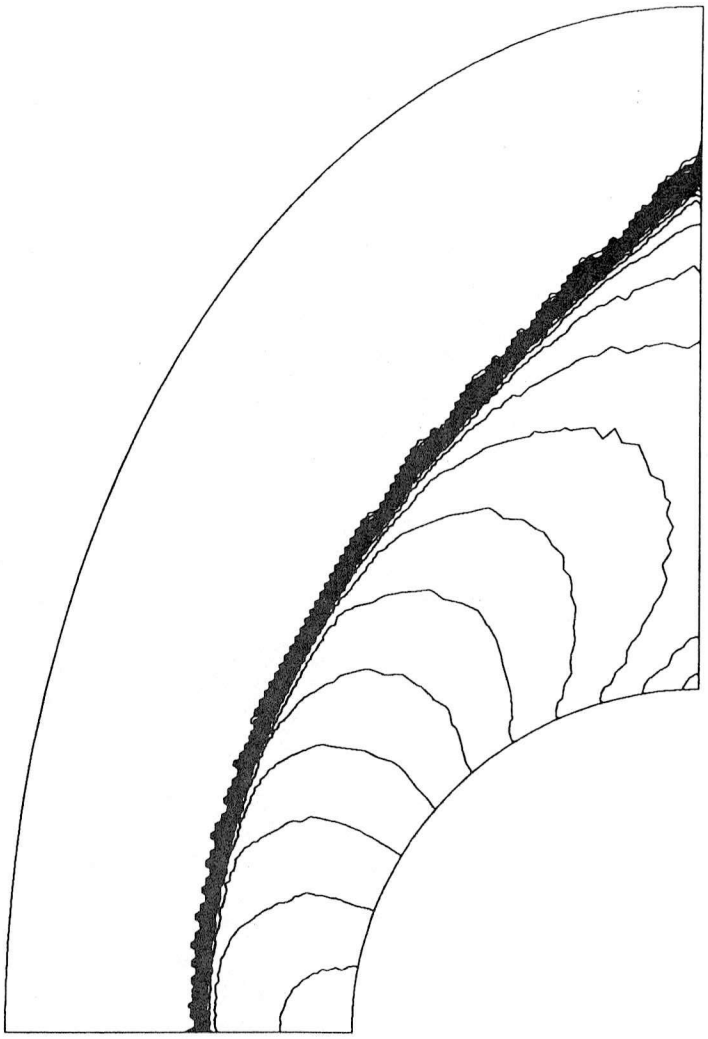

MACH NUMBER CONTOURS

Model: Cylinder Flow
Code : Euler Equation
PGS scheme
Flux : Roe
Order : high-order
Mesh : Fine Mesh
2985 elements
1560 nodes
133 boundary points
Free stream condition :

$M_{inf} = 8.0$

$T_{inf} = 32.6K$

$T_w = 300K$

Figure 10 Cylinder flow (fine mesh) -- Mach contours

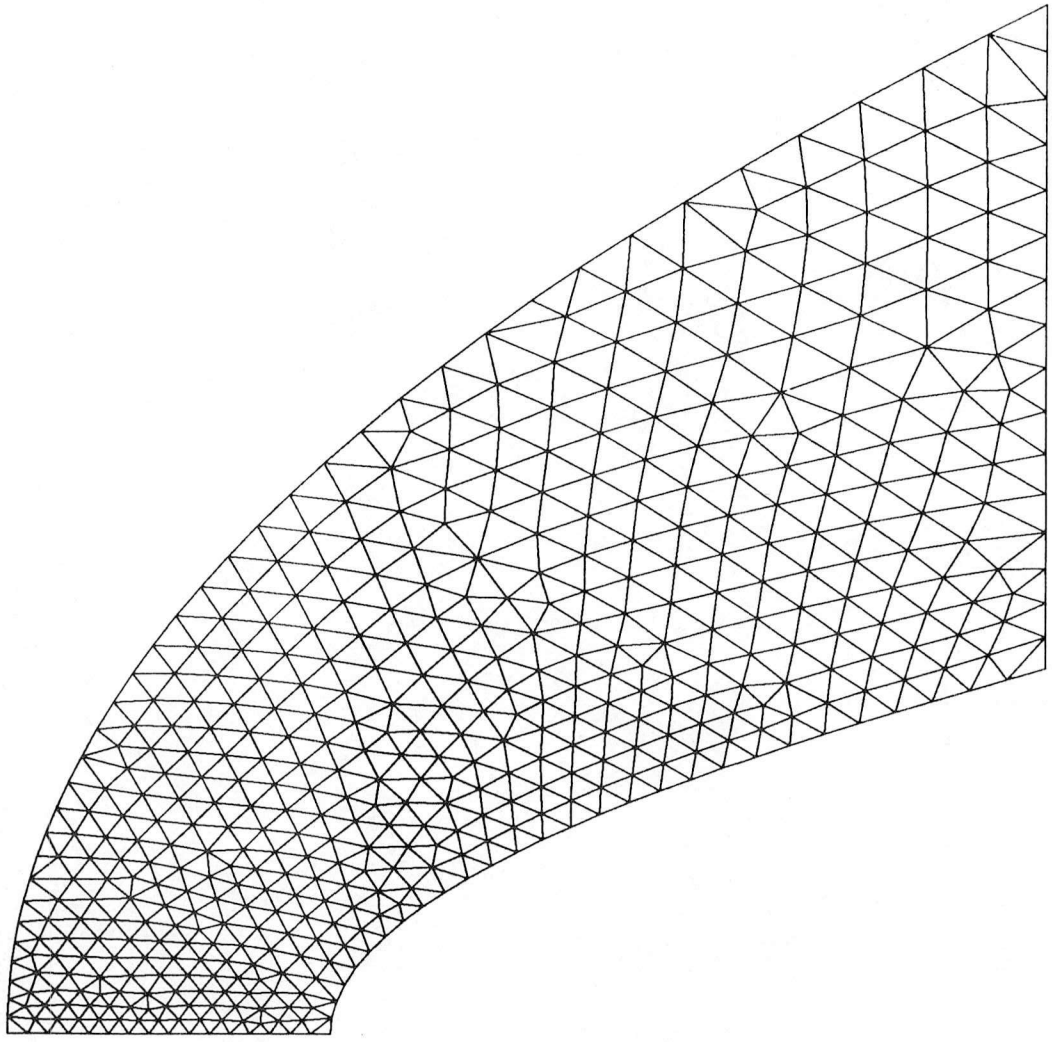

UNSTRUCTURED GRID

Model: Blunt body Flow
Code : Euler Equation
PGS scheme
Flux : Roe
Order : high-order
Mesh : Corse Mesh
899 elements
499 nodes
97 boundary points
Free stream condition :

$M_{inf} = 10.0$

$T_{inf} = 225K$

$T_w = 300K$

Figure 11 Unstructured grid around blunt body (corse mesh)

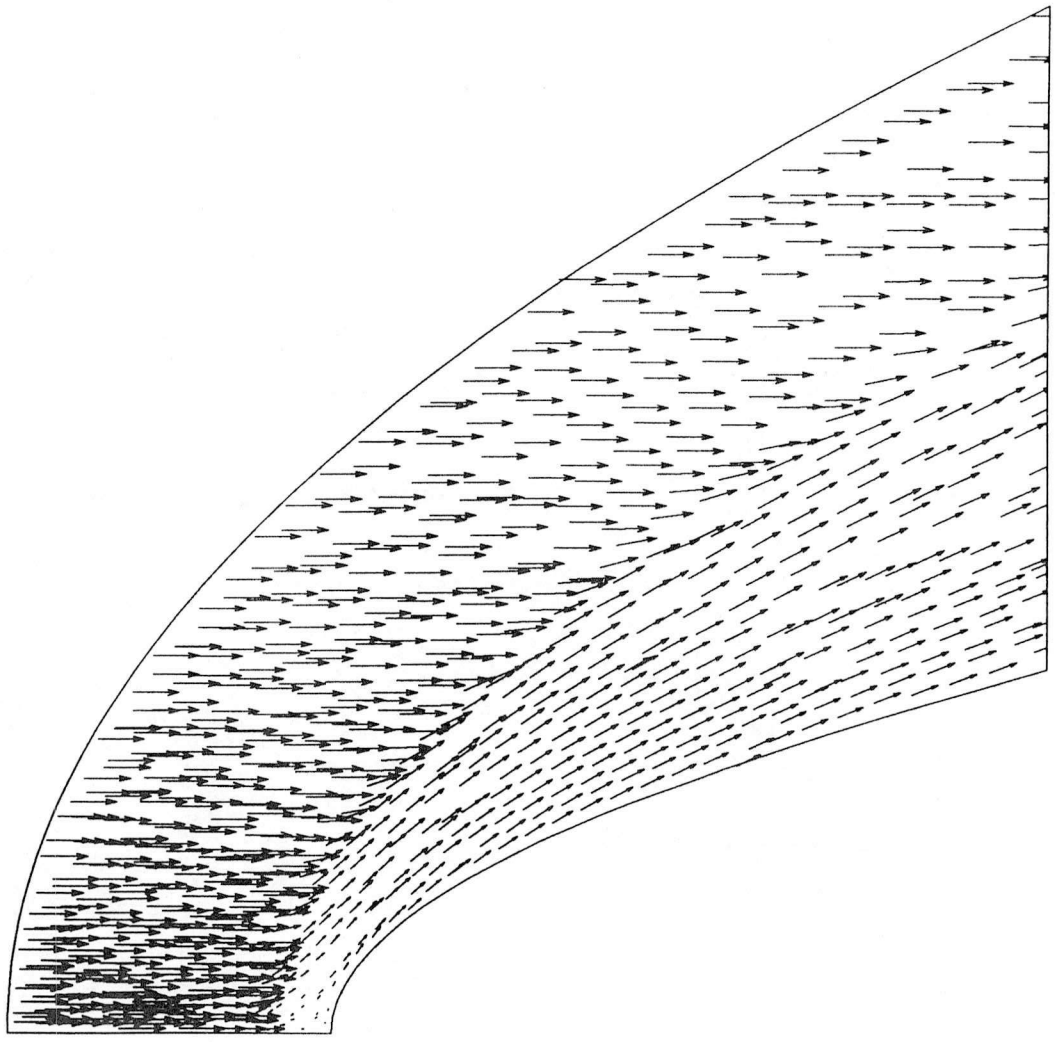

FLOW FIELD

Model: Blunt body Flow
Code : Euler Equation
PGS scheme
Flux : Roe
Order : high-order
Mesh : Corse Mesh
899 elements
499 nodes
97 boundary points
Free stream condition :

$M_{inf} = 10.0$

$T_{inf} = 225K$

$T_w = 300K$

Figure 12 Blunt body flow (coarse mesh) -- Velocity field

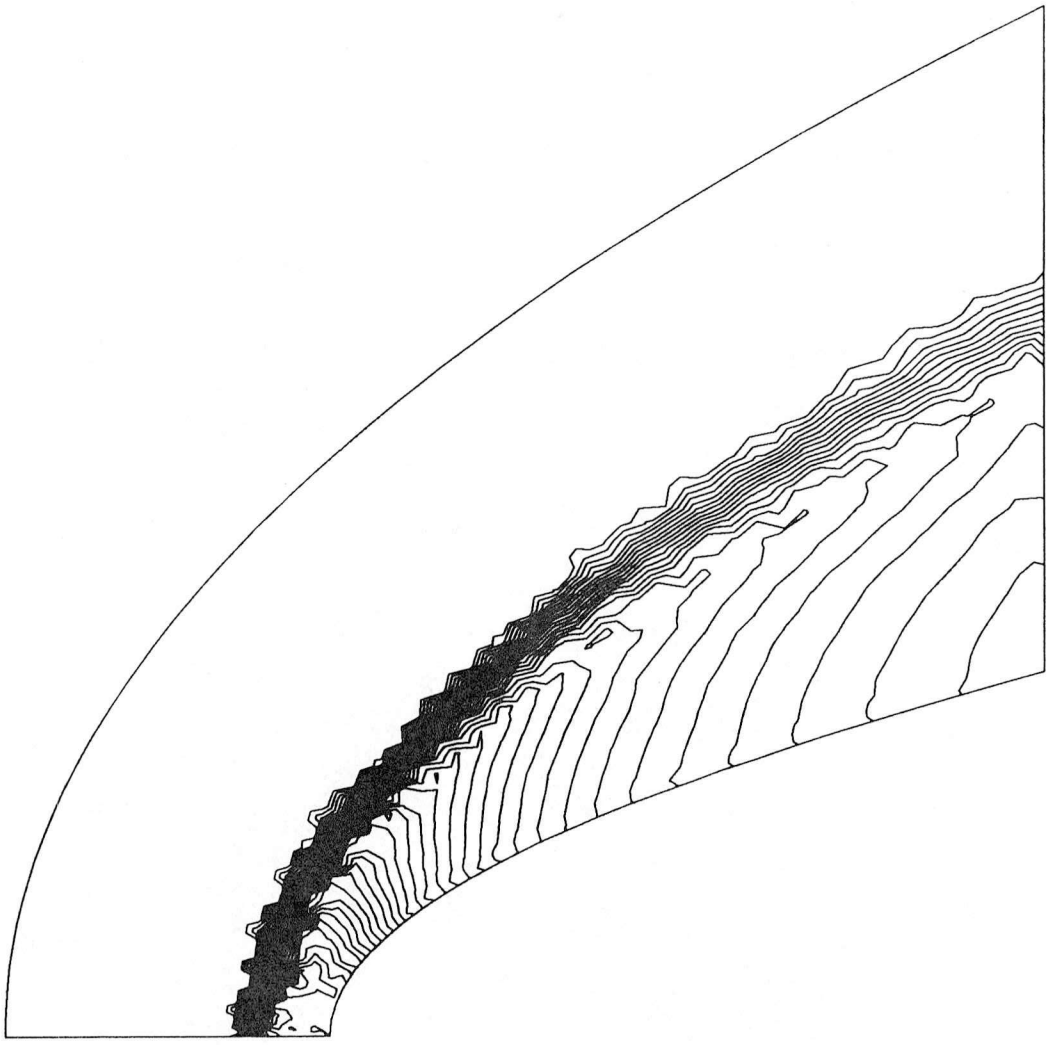

PRESSURE CONTOURS

Model: Blunt body Flow
Code : Euler Equation
PGS scheme
Flux : Roe
Order : high-order
Mesh : Coarse Mesh
899 elements
499 nodes
97 boundary points
Free stream condition :

$M_{inf} = 10.0$

$T_{inf} = 225K$

$T_w = 300K$

Figure 13 Cylinder flow (coarse mesh) -- Pressure contours

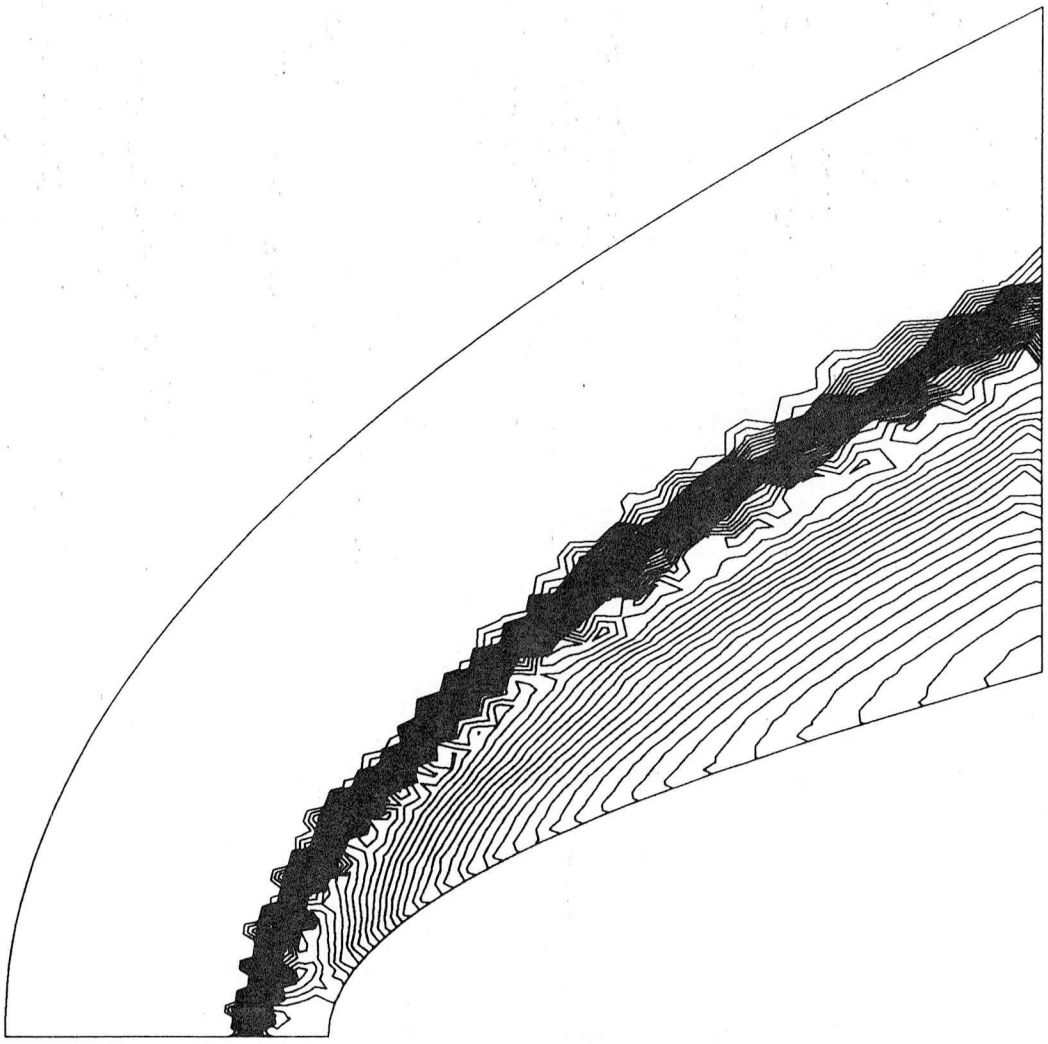

DENSITY CONTOURS

Model: Blunt body Flow
Code : Euler Equation
PGS scheme
Flux : Roe
Order : high-order
Mesh : Coarse Mesh
899 elements
499 nodes
97 boundary points
Free stream condition :

$M_{\inf} = 10.0$

$T_{\inf} = 225K$

$T_w = 300K$

Figure 14 Blunt body flow (coarse mesh) -- Density contours

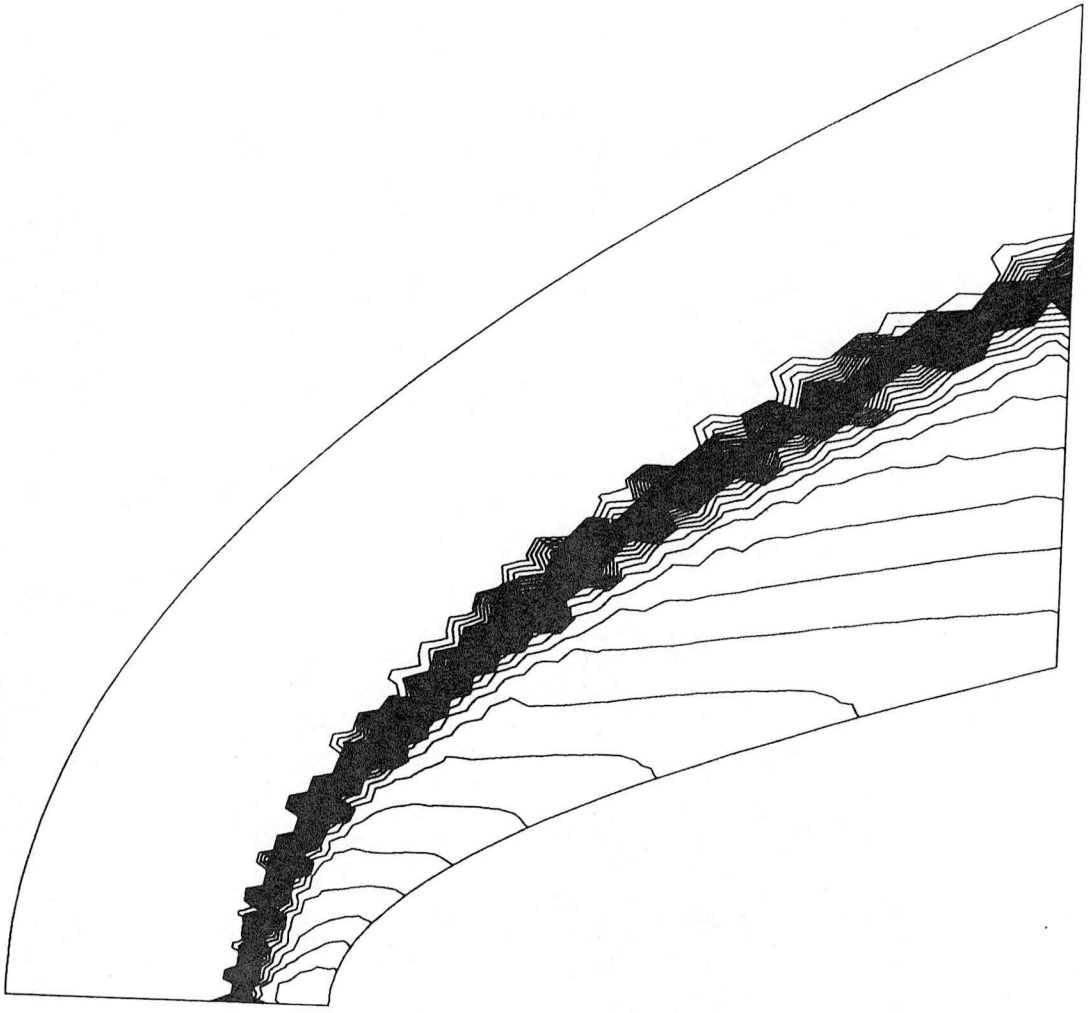

MACH NUMBER CONTOURS

Model: Blunt body Flow
Code : Euler Equation
PGS scheme
Flux : Roe
Order : high-order
Mesh : Coarse Mesh
899 elements
499 nodes
97 boundary points
Free stream condition :

$M_{inf} = 10.0$

$T_{inf} = 225K$

$T_w = 300K$

Figure 15 Cylinder flow (coarse mesh) -- Mach contours

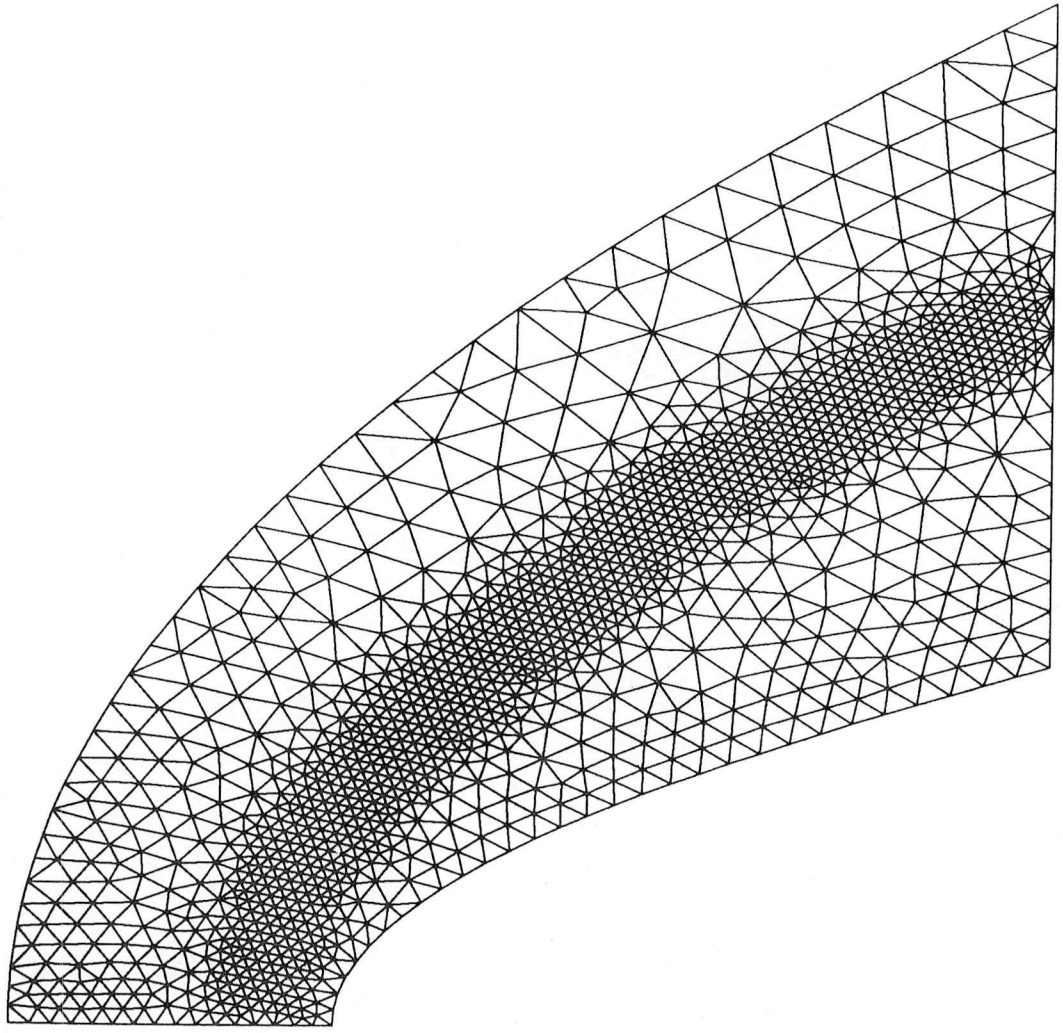

UNSTRUCTURED GRID

Model: Blunt body Flow
Code : Euler Equation
PGS scheme
Flux : Roe
Order : high-order
Mesh : Fine Mesh
2697 elements
1400 nodes
101 boundary points
Free stream condition :

$M_{inf} = 10.0$

$T_{inf} = 225K$

$T_w = 300K$

Figure 16 Unstructured grid around blunt body (fine mesh)

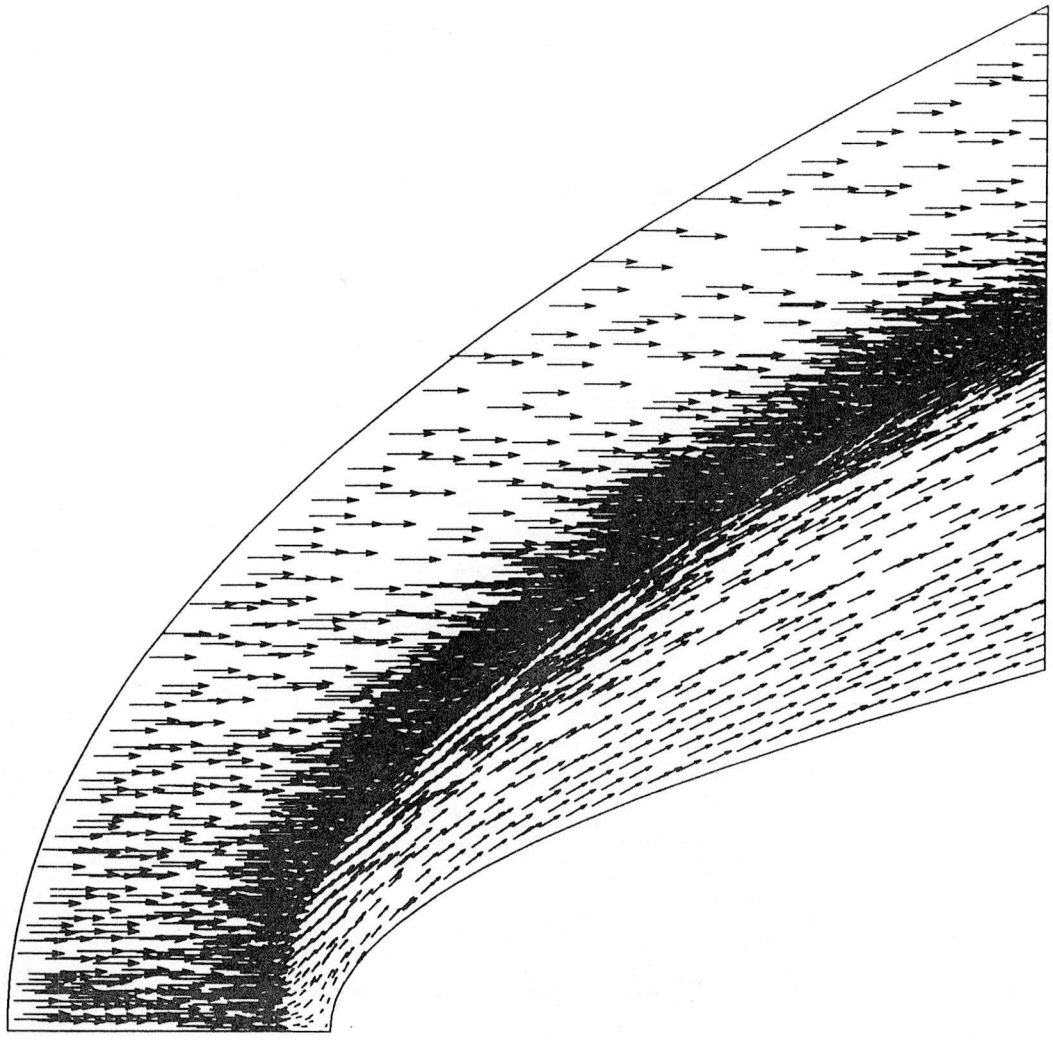

FLOW FIELD

Model: Blunt body Flow
Code : Euler Equation
PGS scheme
Flux : Roe
Order : high-order
Mesh : Fine Mesh
2697 elements
1400 nodes
101 boundary points
Free stream condition :

$M_{inf} = 10.0$

$T_{inf} = 225K$

$T_w = 300K$

Figure 17(a) Blunt body flow (fine mesh) -- Velocity field

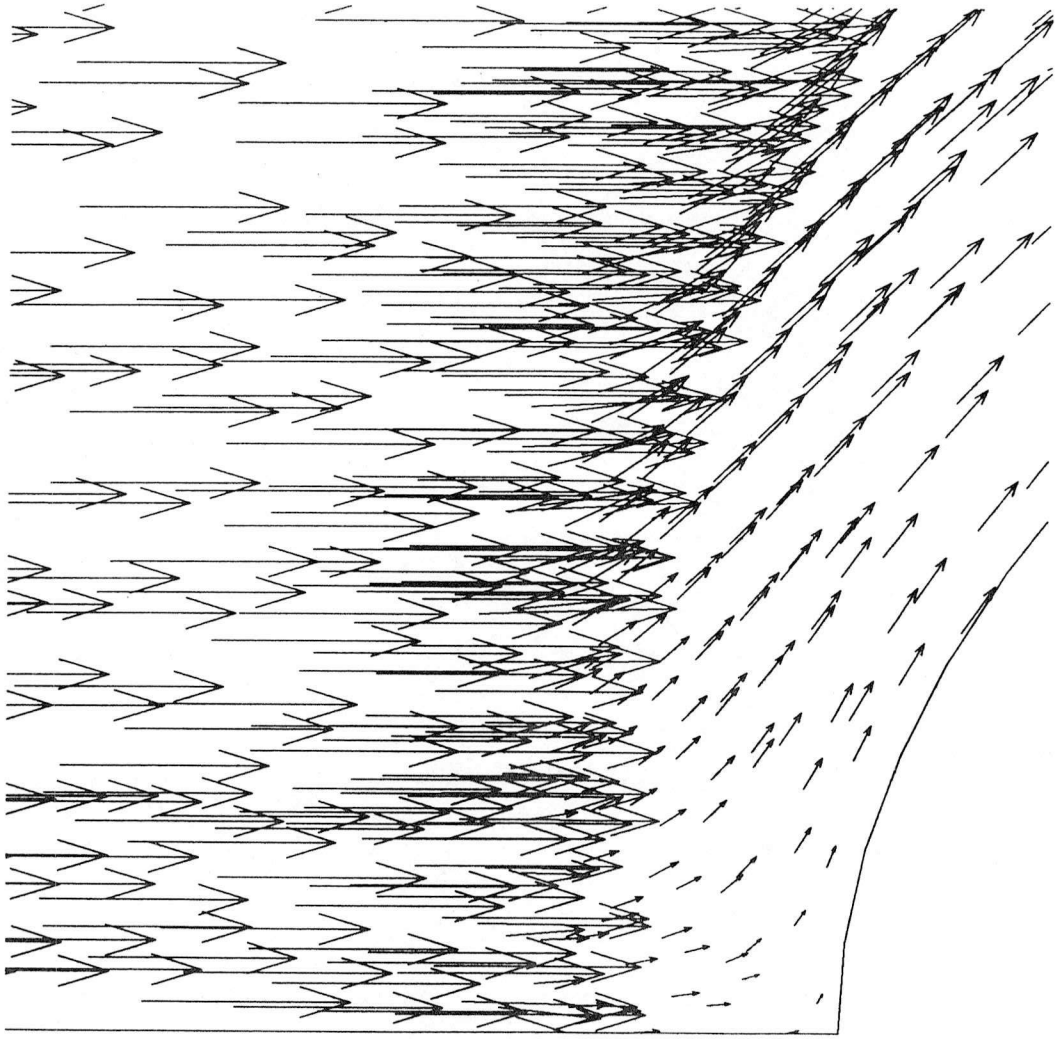

FLOW FIELD

Model: Blunt body Flow
Code : Euler Equation
PGS scheme
Flux : Roe
Order : high-order
Mesh : Fine Mesh
2697 elements
1400 nodes
101 boundary points
Free stream condition :

$M_{inf} = 10.0$

$T_{inf} = 225K$

$T_w = 300K$

Figure 17(b) Blunt body flow (fine mesh) -- Velocity field

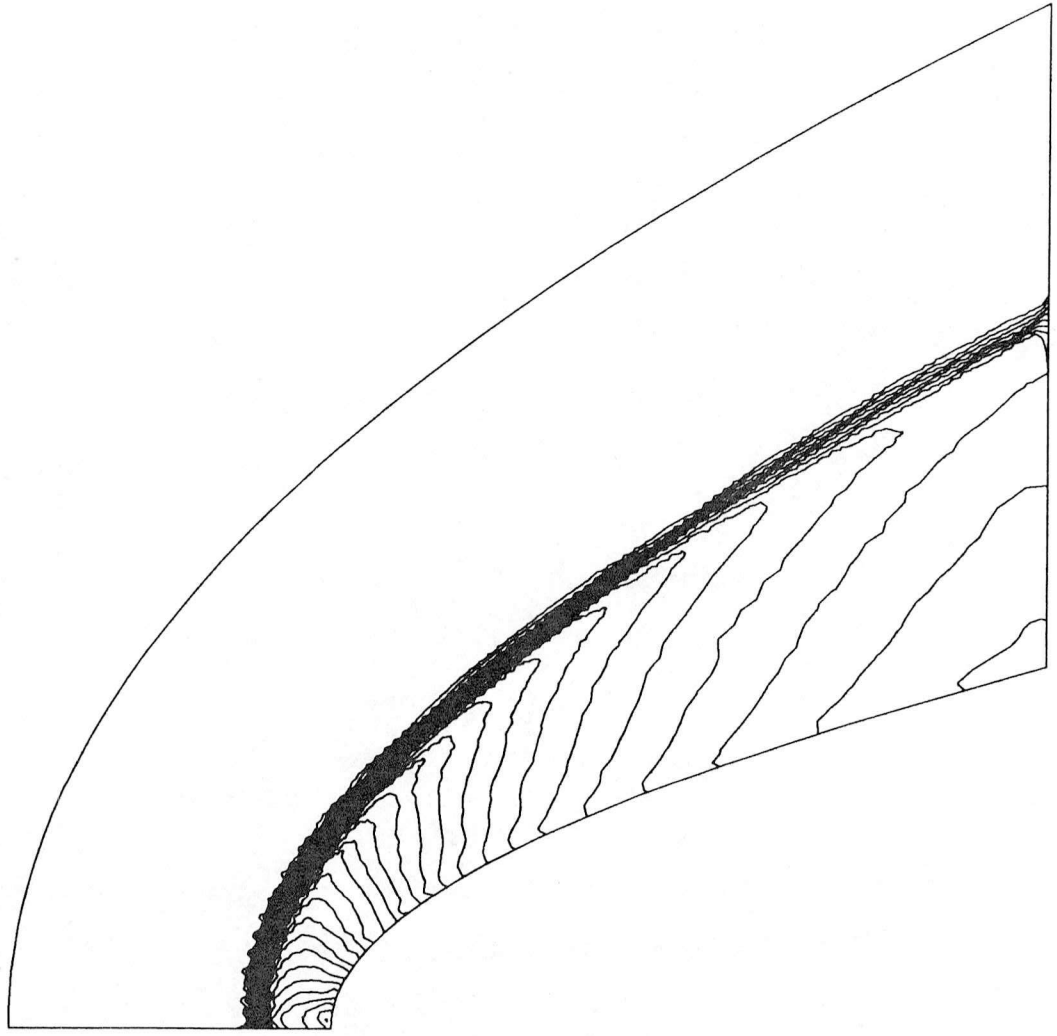

PRESSURE CONTOURS

Model: Blunt body Flow
Code : Euler Equation
PGS scheme
Flux : Roe
Order : high-order
Mesh : Fine Mesh
2697 elements
1400 nodes
101 boundary points
Free stream condition :

$M_{inf} = 10.0$

$T_{inf} = 225K$

$T_w = 300K$

Figure 18 Blunt body flow (fine mesh) -- Pressure contours

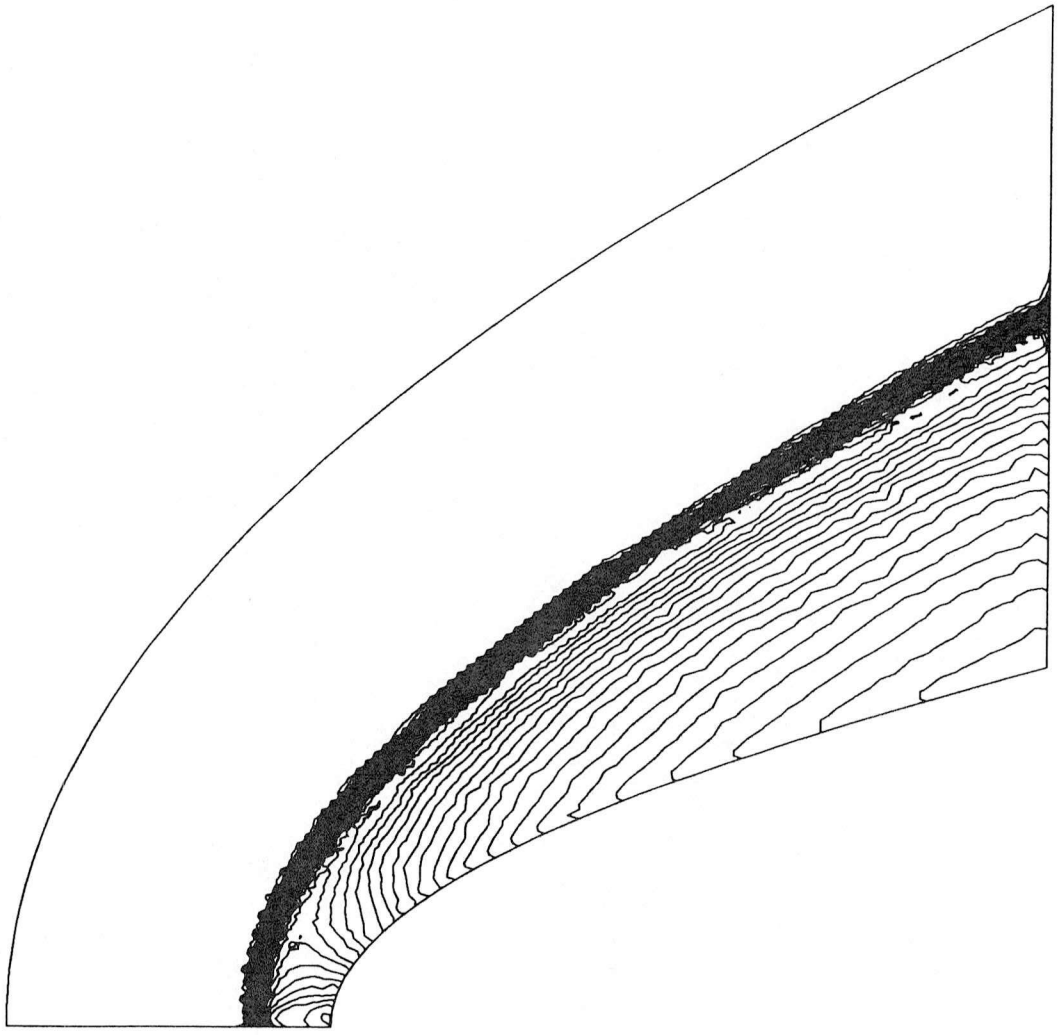

DENSITY CONTOURS

Model: Blunt body Flow
Code : Euler Equation
PGS scheme
Flux : Roe
Order : high-order
Mesh : Fine Mesh
2697 elements
1400 nodes
101 boundary points
Free stream condition :

$M_{inf} = 10.0$

$T_{inf} = 225K$

$T_w = 300K$

Figure 19 Blunt body flow (fine mesh) -- Density contours

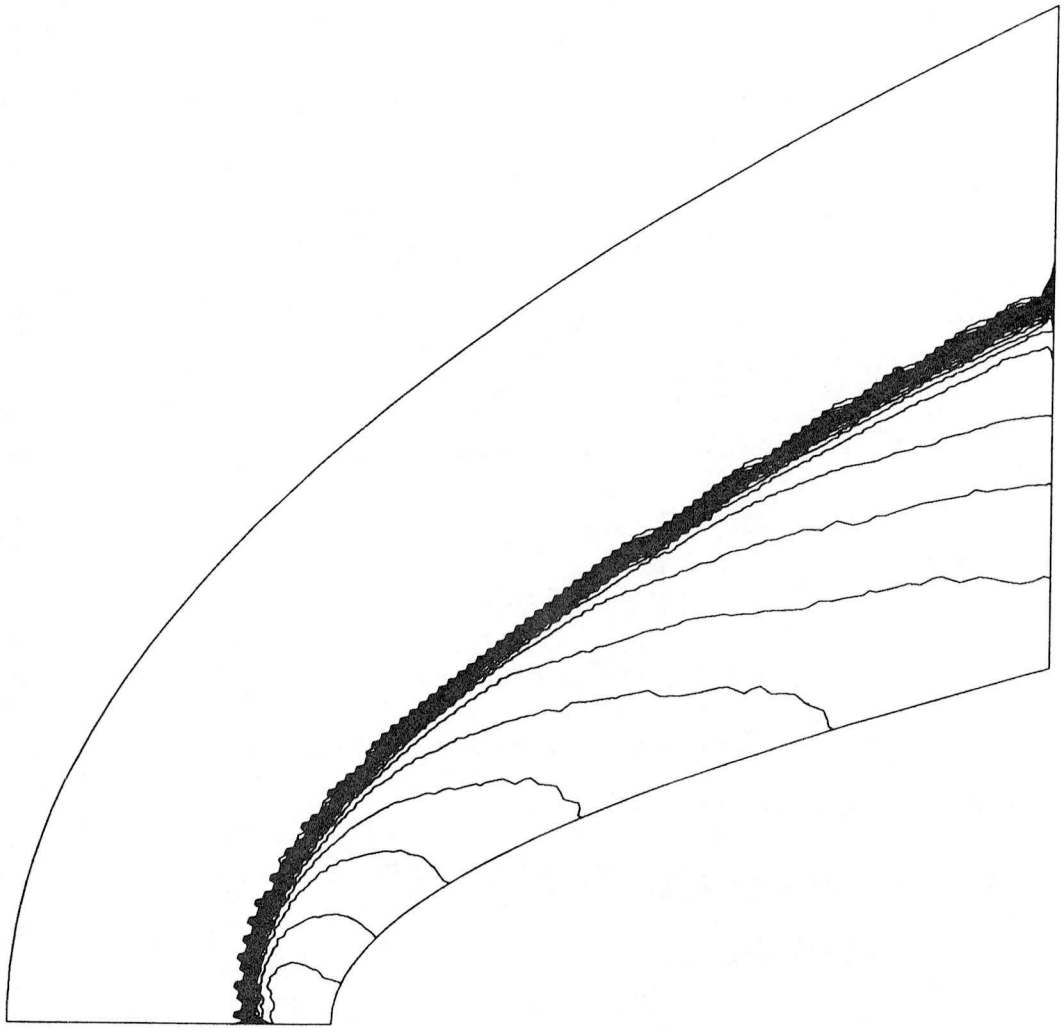

MACH NUMBER CONTOURS

Model: Blunt body Flow
Code : Euler Equation
PGS scheme
Flux : Roe
Order : high-order
Mesh : Fine Mesh
2697 elements
1400 nodes
101 boundary points
Free stream condition :

$M_{inf} = 10.0$

$T_{inf} = 225K$

$T_w = 300K$

Figure 20 Blunt body flow (fine mesh) -- Mach contours

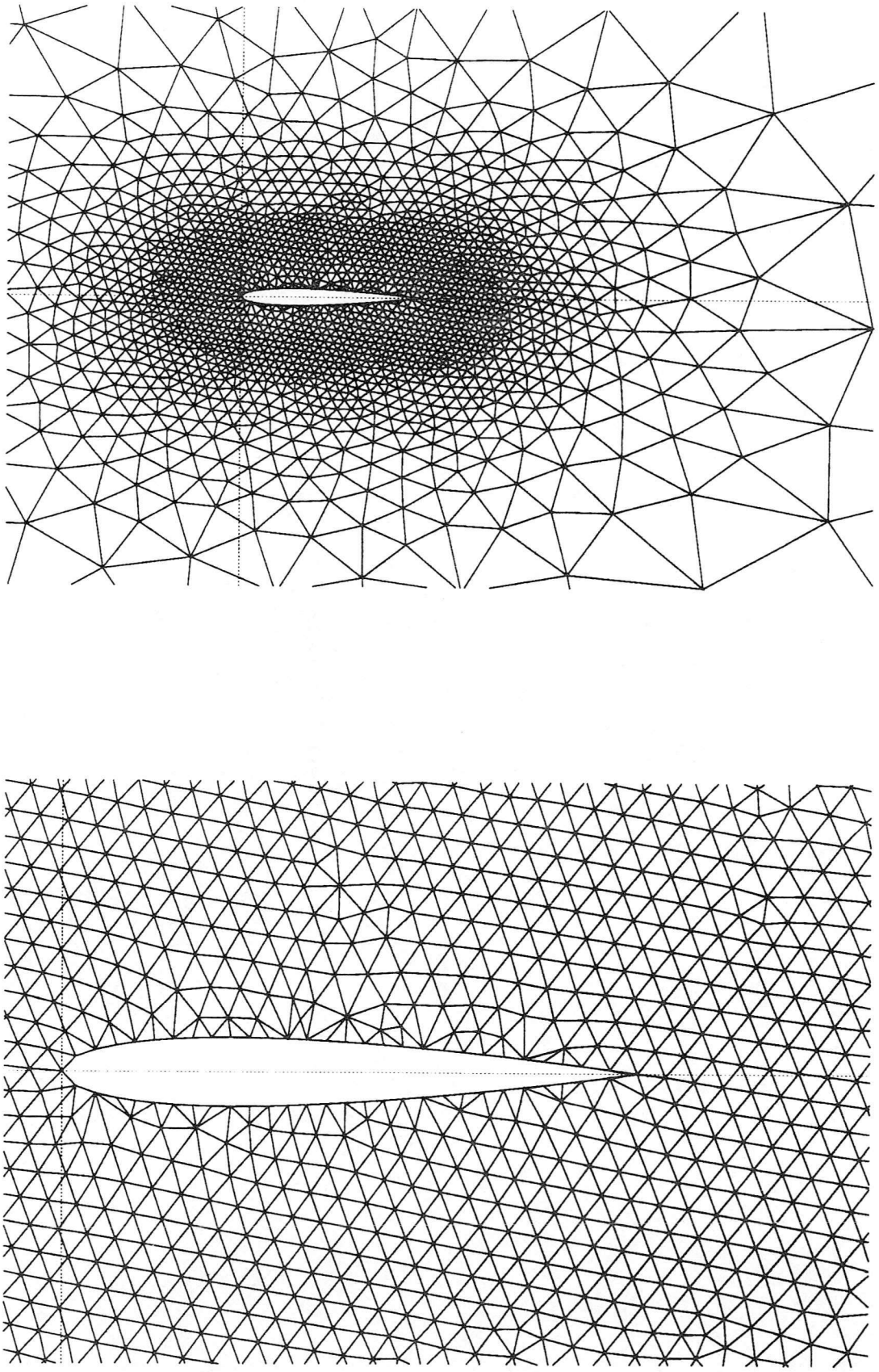

Figure 21 NACA 0012 Airfoil
Mesh 1 --- first triangulation of airfoil
3246 elements 1670 nodes

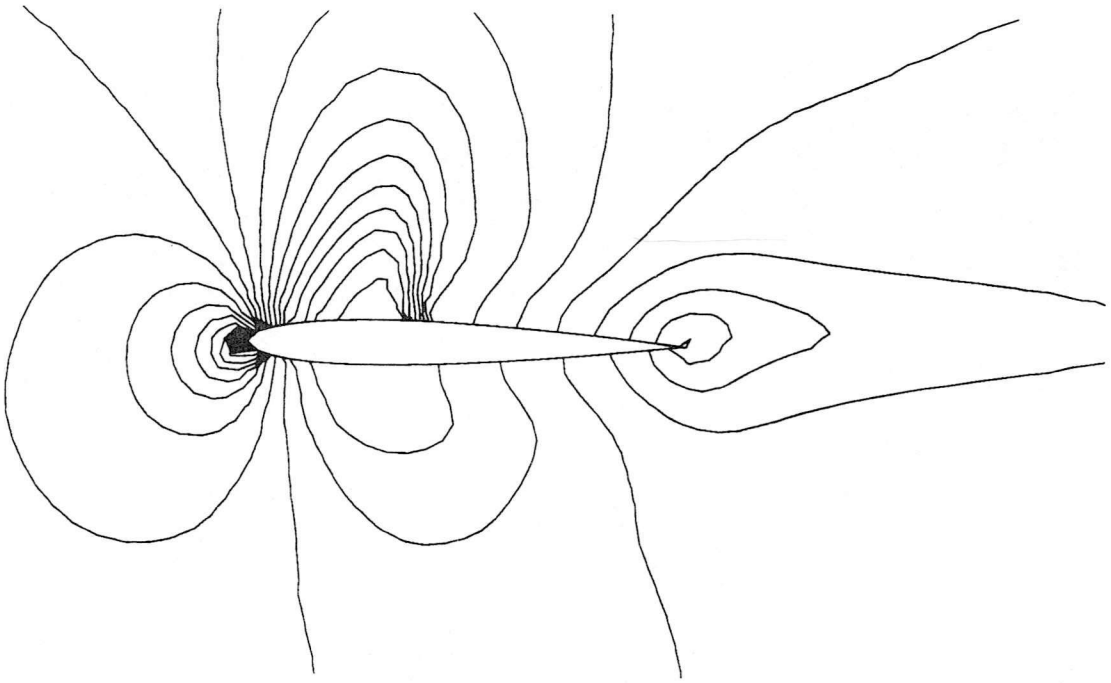

Figure 22(a) NACA 0012 Airfoil
Mach number contours on Mesh1
Mach=0.75 Alp=2.0 (Deg)

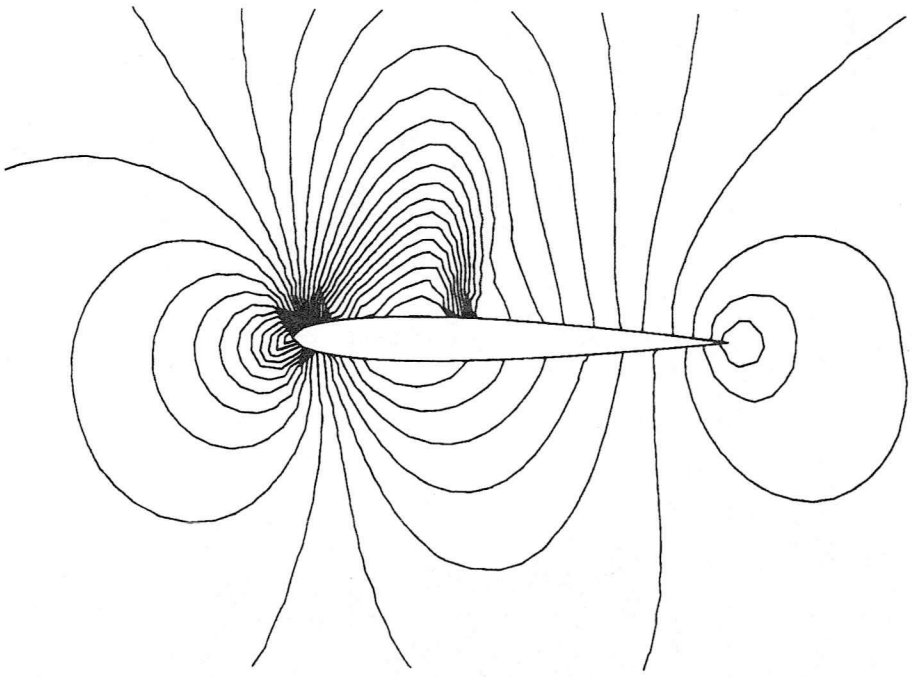

Figure 22(b) NACA 0012 Airfoil
Pressure contours on Mesh1
Mach=0.75 Alp=2.0 (Deg)

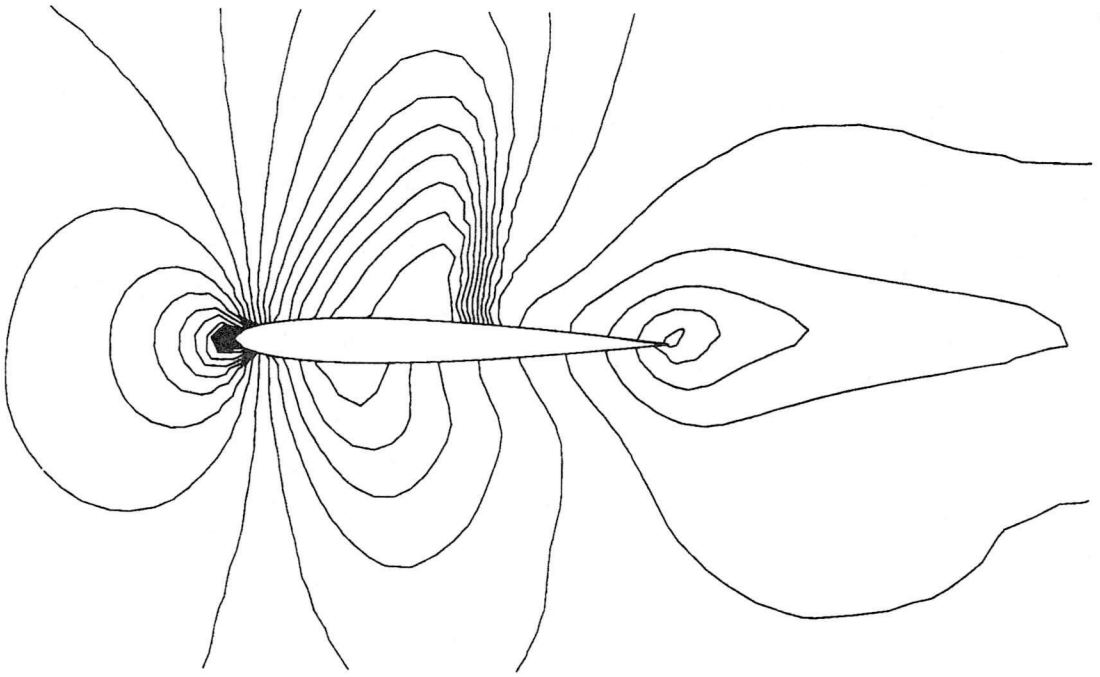

Figure 23(a) NACA 0012 Airfoil
Mach number contours on Mesh1
Mach=0.80 Alp=1.25 (Deg)

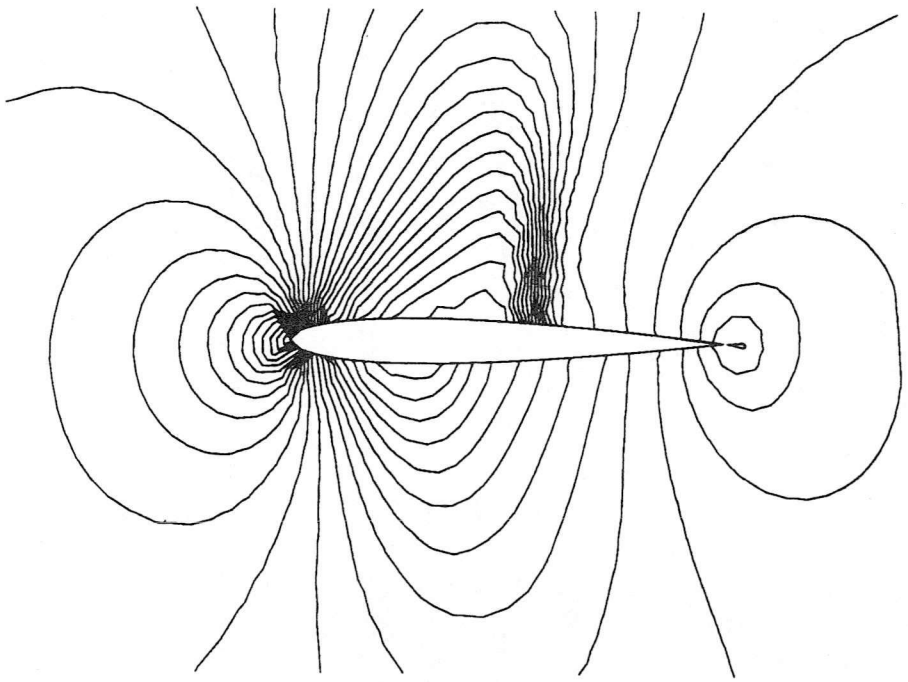

Figure 23(b) NACA 0012 Airfoil
Pressure contours on Mesh1
Mach=0.80 Alp=1.25 (Deg)

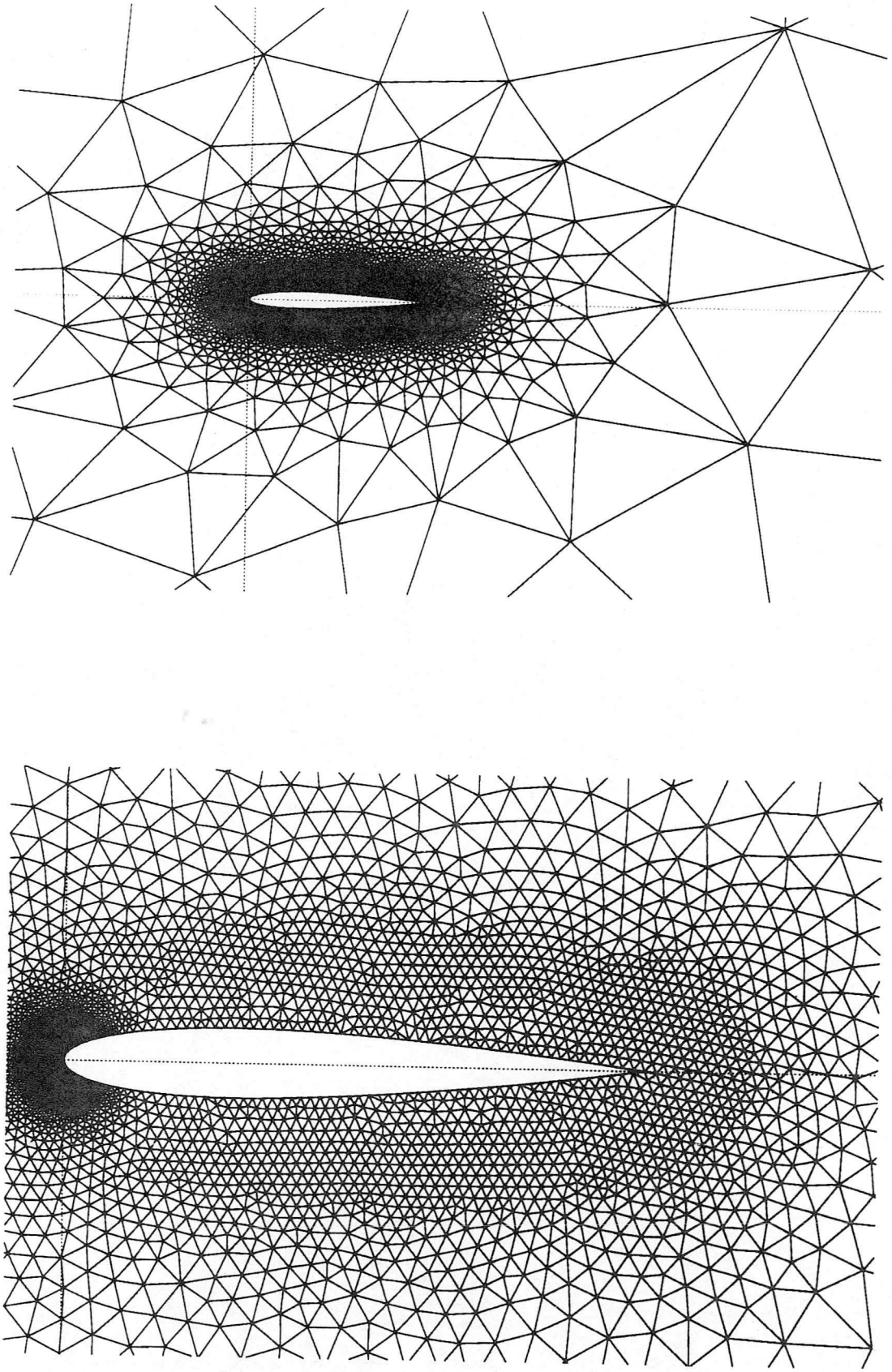

Figure 24 NACA 0012 Airfoil
Mesh 2 --- second triangulation of airfoil
6354 elements 3267 nodes

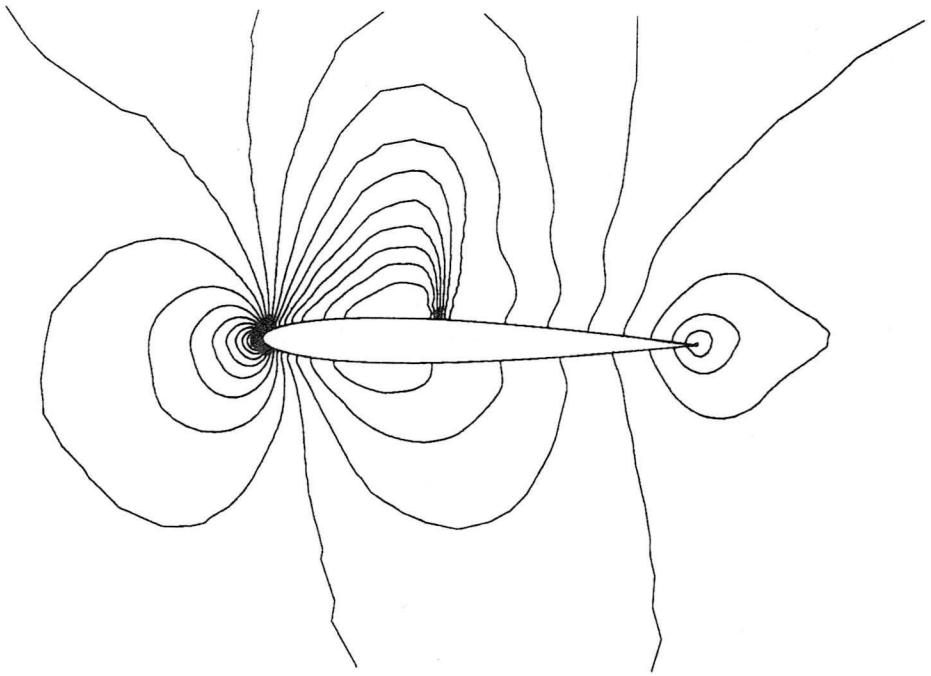

Figure 25(a) NACA 0012 Airfoil
Mach number contours on Mesh2
Mach=0.75 Alp=2.0 (Deg)

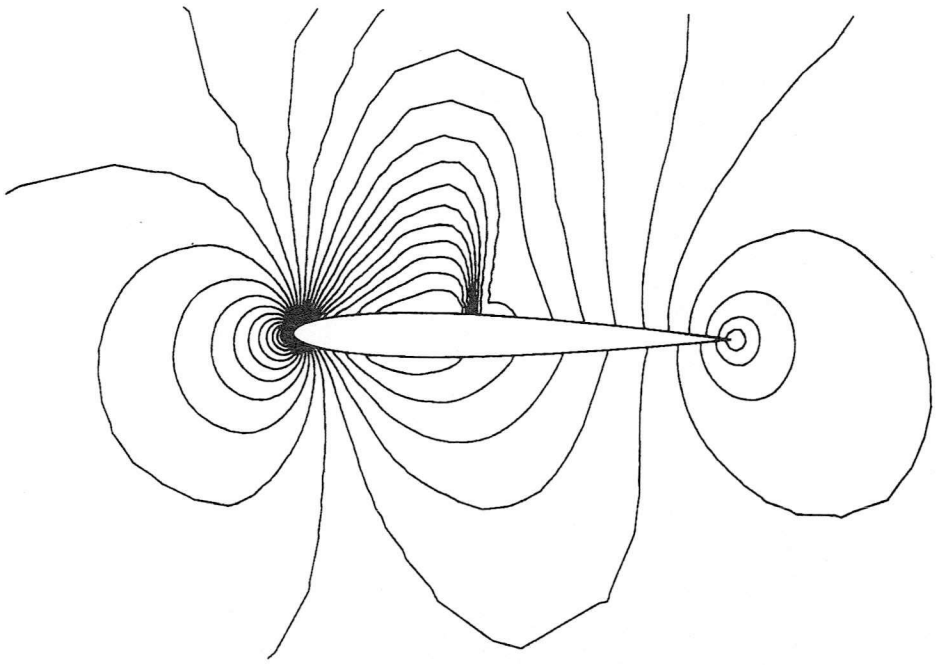

Figure 25(b) NACA 0012 Airfoil
Pressure contours on Mesh2
Mach=0.75 Alp=2.0 (Deg)

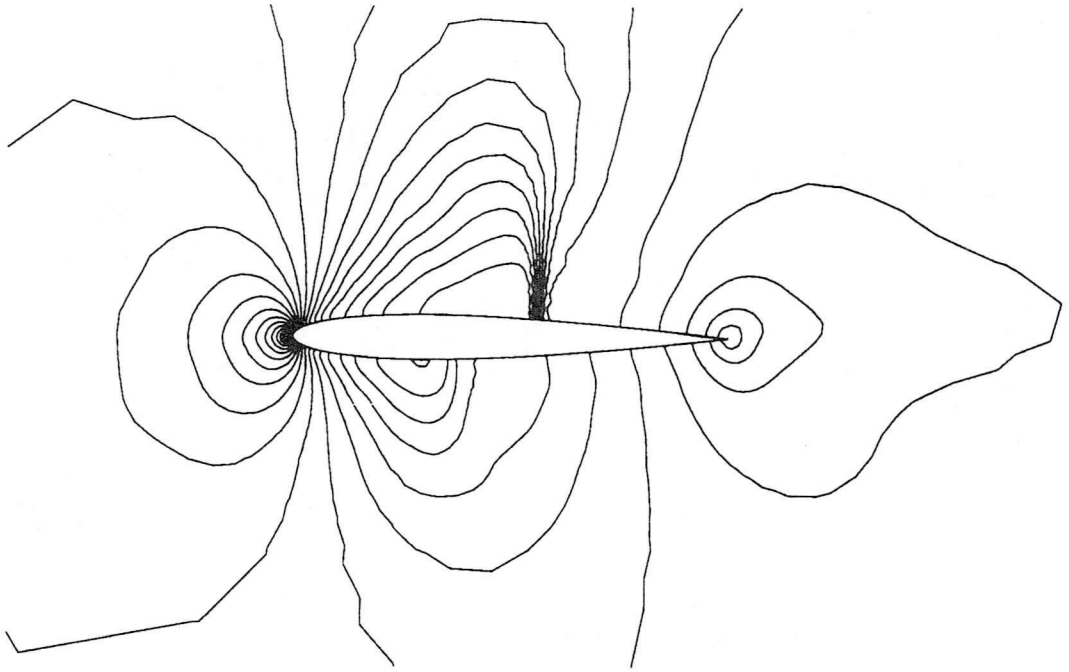

Figure 26(a) NACA 0012 Airfoil
Mach number contours on Mesh2
Mach=0.80 Alp=1.25 (Deg)

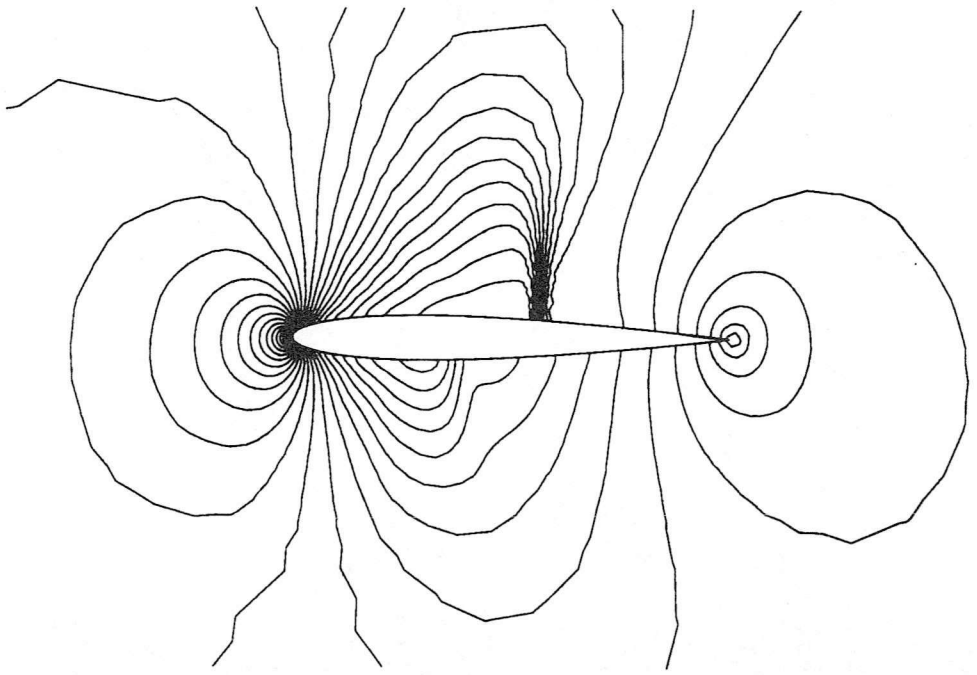

Figure 26(b) NACA 0012 Airfoil
Pressure contours on Mesh2
Mach=0.80 Alp=1.25 (Deg)

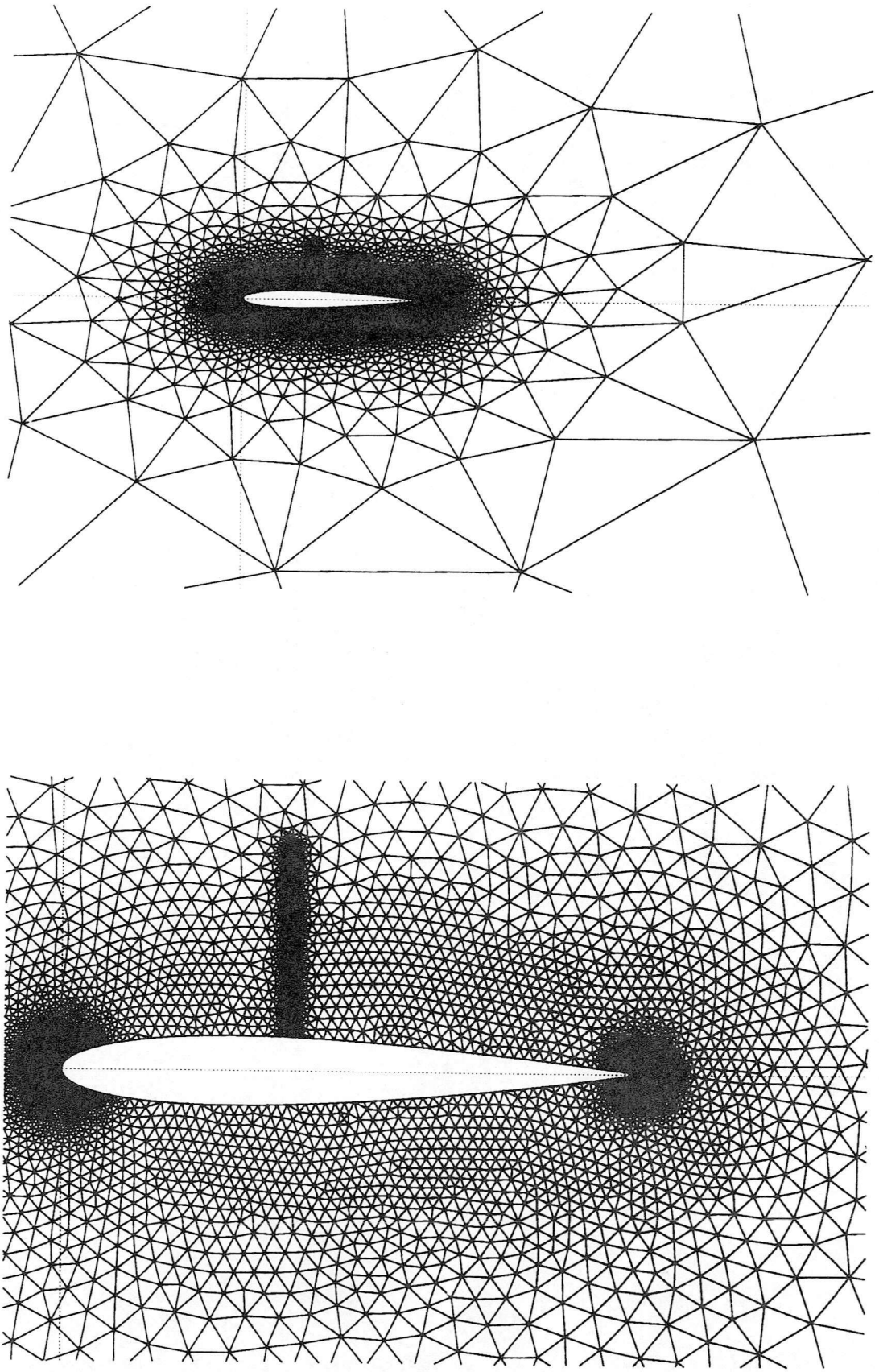

Figure 27 NACA 0012 Airfoil
Mesh 3 --- adaptive triangulation of airfoil on case (Mach=0.75 Alp=2.0)
8558 elements 4381 nodes

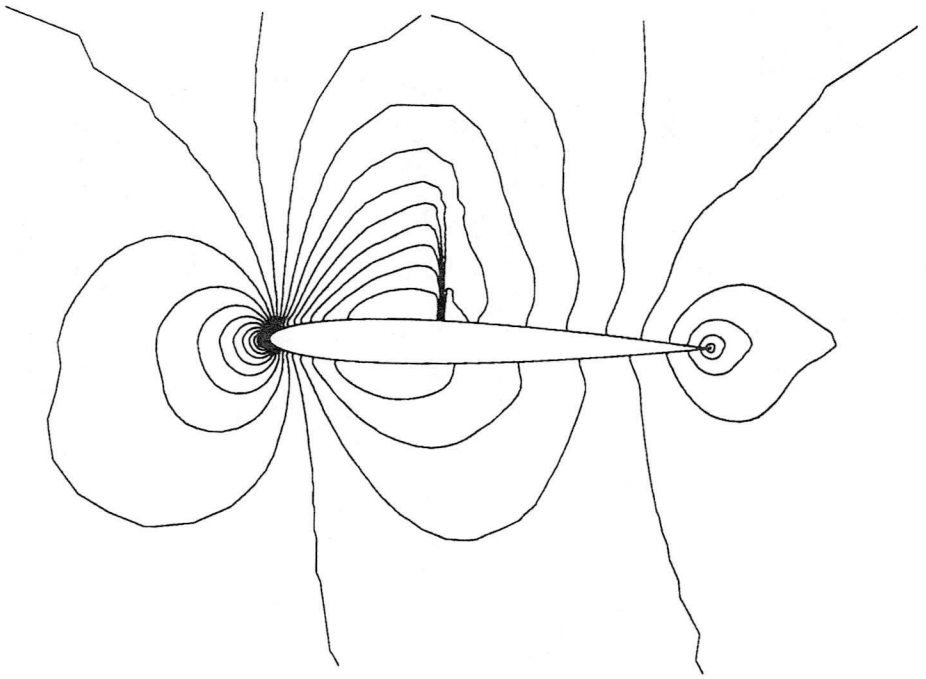

Figure 28(a) NACA 0012 Airfoil
Mach number contours on Mesh3
Mach=0.75 Alp=2.0 (Deg)
first-order results

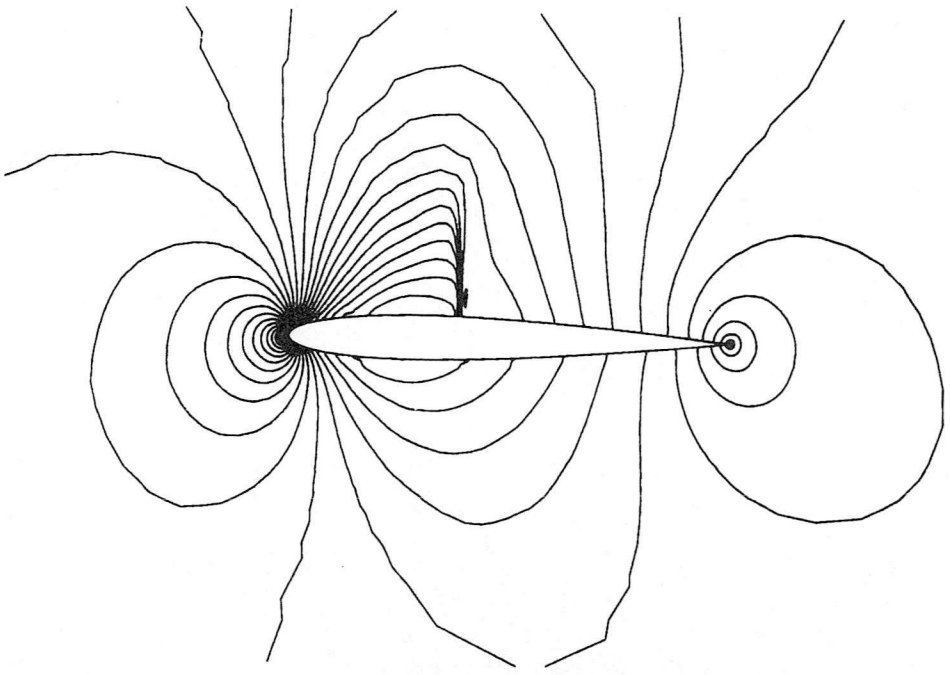

Figure 28(b) NACA 0012 Airfoil
Pressure contours on Mesh3
Mach=0.75 Alp=2.0 (Deg)
first-order results

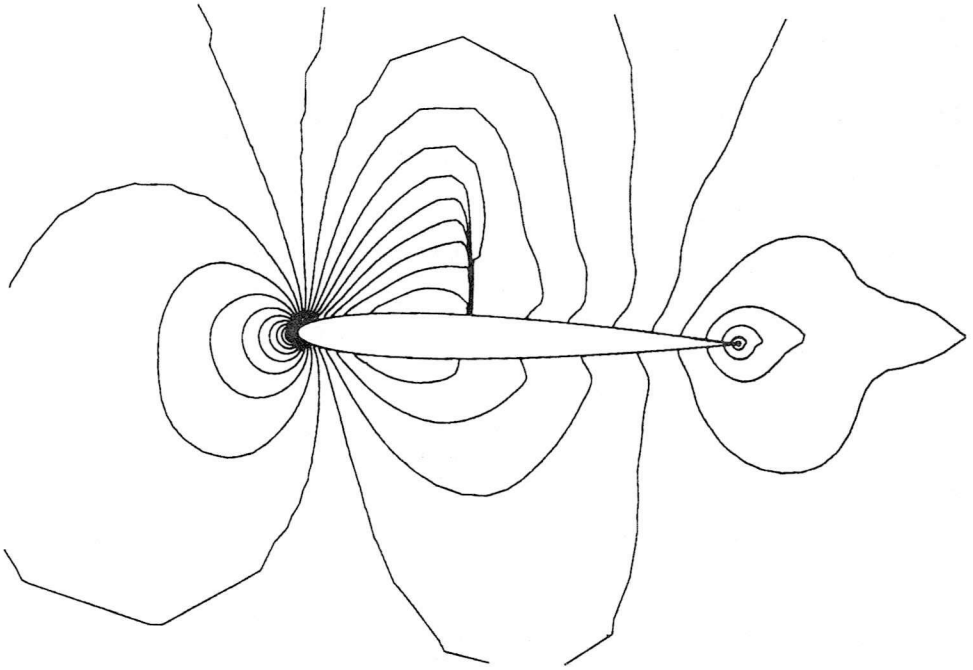

Figure 29(a) NACA 0012 Airfoil
Mach number contours on Mesh3
Mach=0.75 Alp=2.0 (Deg)
second-order results

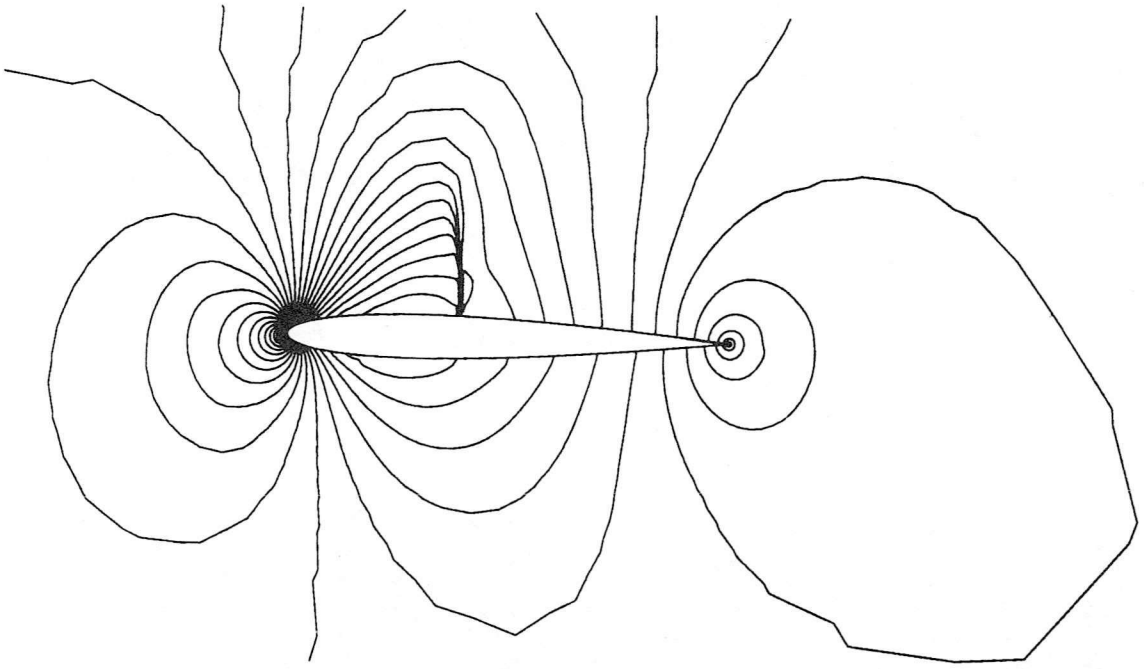

Figure 29(b) NACA 0012 Airfoil
Pressure contours on Mesh3
Mach=0.75 Alp=2.0 (Deg)
second-order results

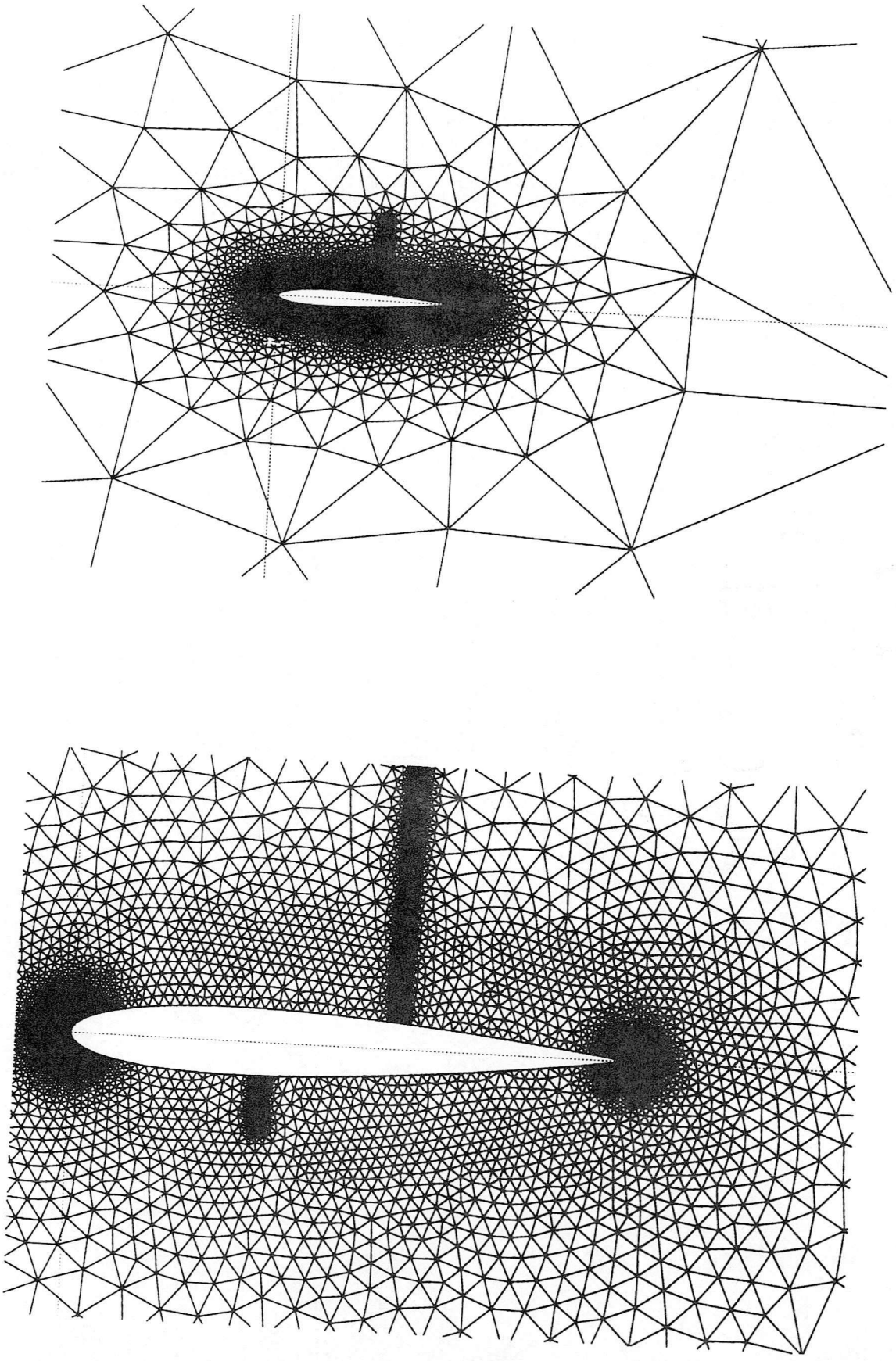

Figure 30 NACA 0012 Airfoil
Mesh 3 --- adaptive triangulation of airfoil on case (Mach=0.80 Alp=1.25)
9769 elements 4988 nodes

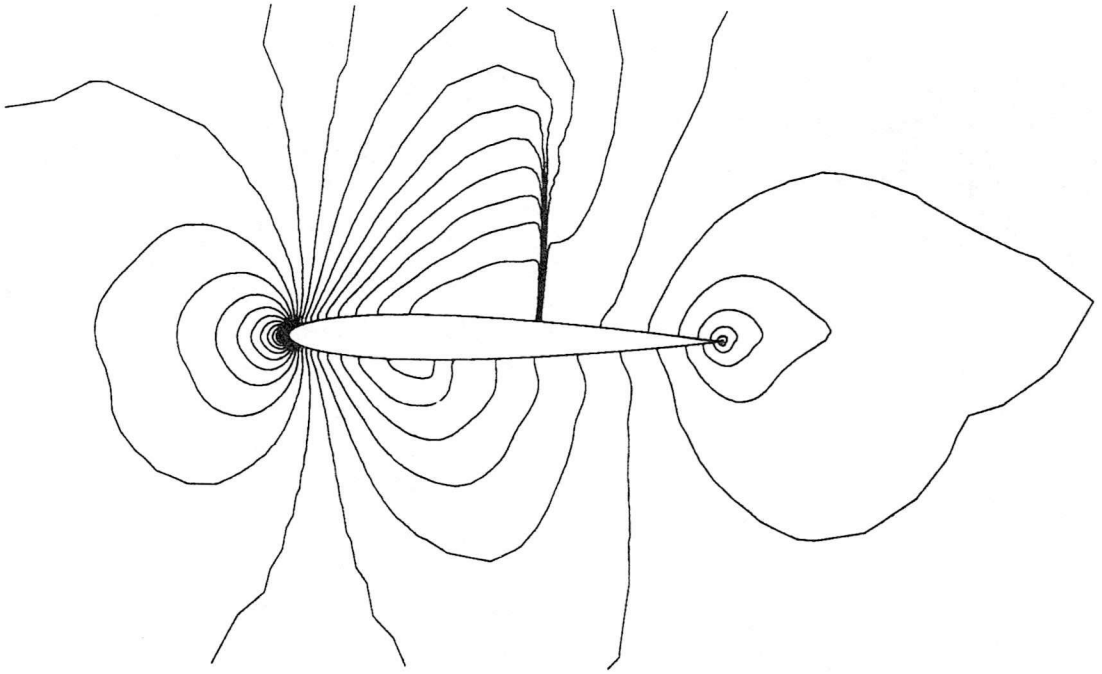

Figure 31(a) NACA 0012 Airfoil
Mach number contours on Mesh3
Mach=0.80 Alp=1.25 (Deg)
first-order results

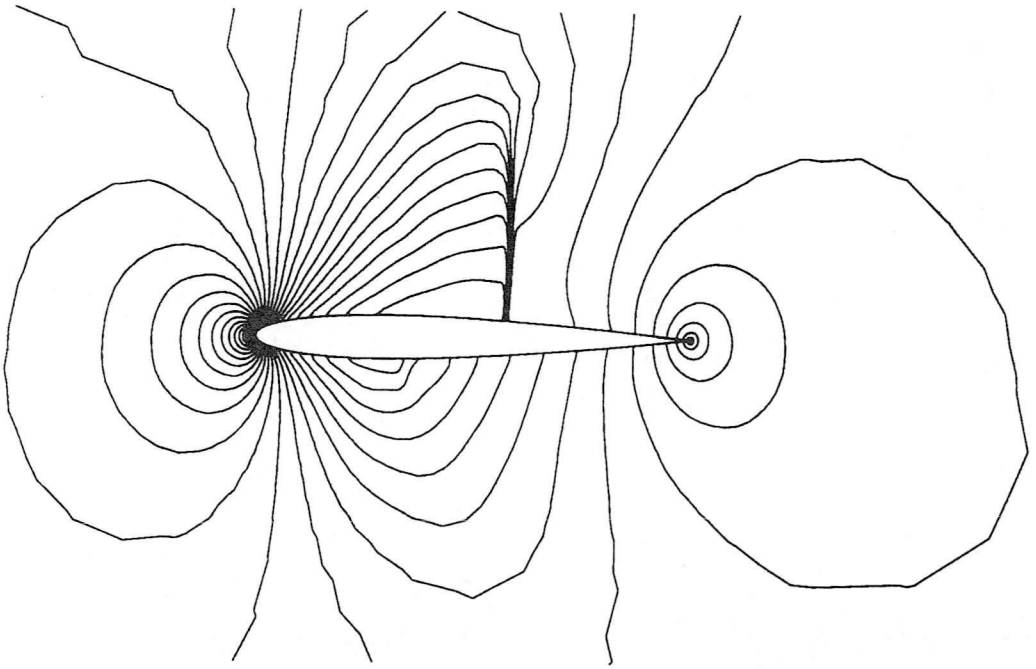

Figure 31(b) NACA 0012 Airfoil
Pressure contours on Mesh3
Mach=0.80 Alp=1.25 (Deg)
first-order results

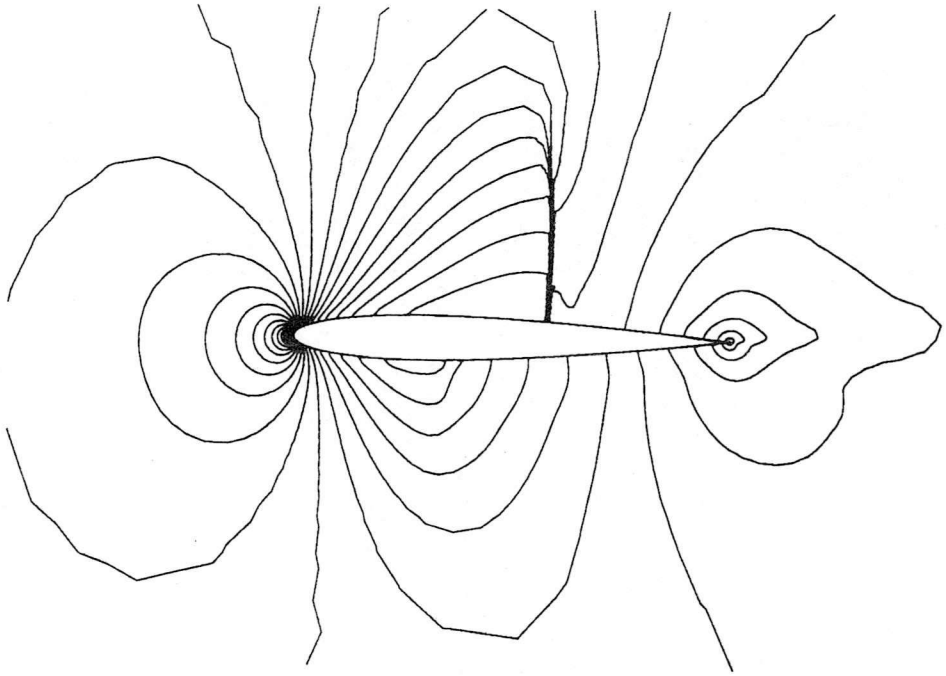

Figure 32(a) NACA 0012 Airfoil
Mach number contours on Mesh3
Mach=0.80 Alp=1.25 (Deg)
second-order results

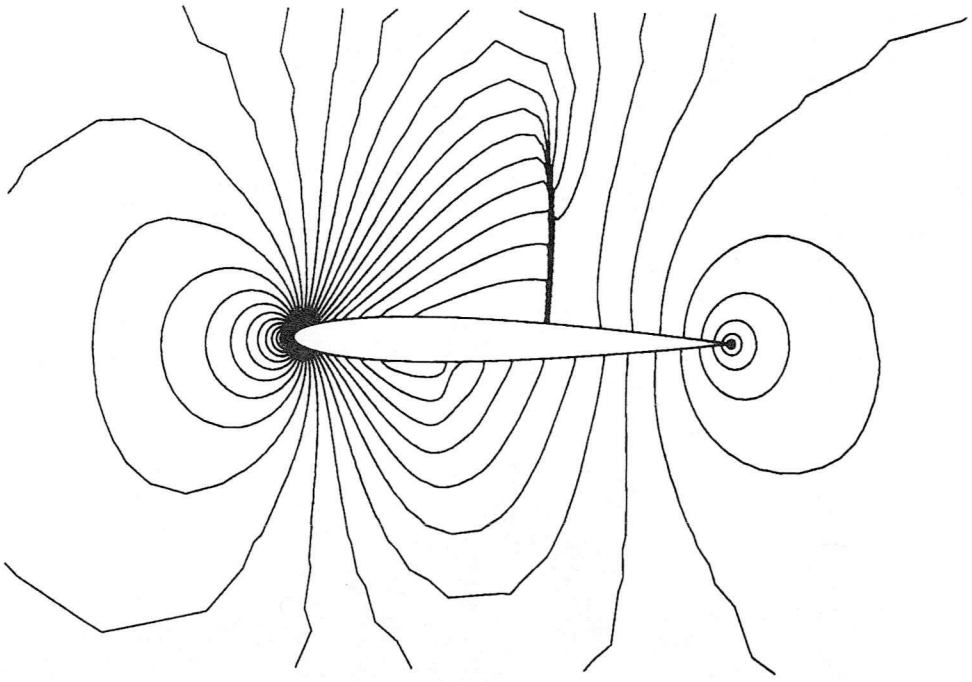

Figure 32(b) NACA 0012 Airfoil
Pressure contours on Mesh3
Mach=0.80 Alp=1.25 (Deg)
second-order results

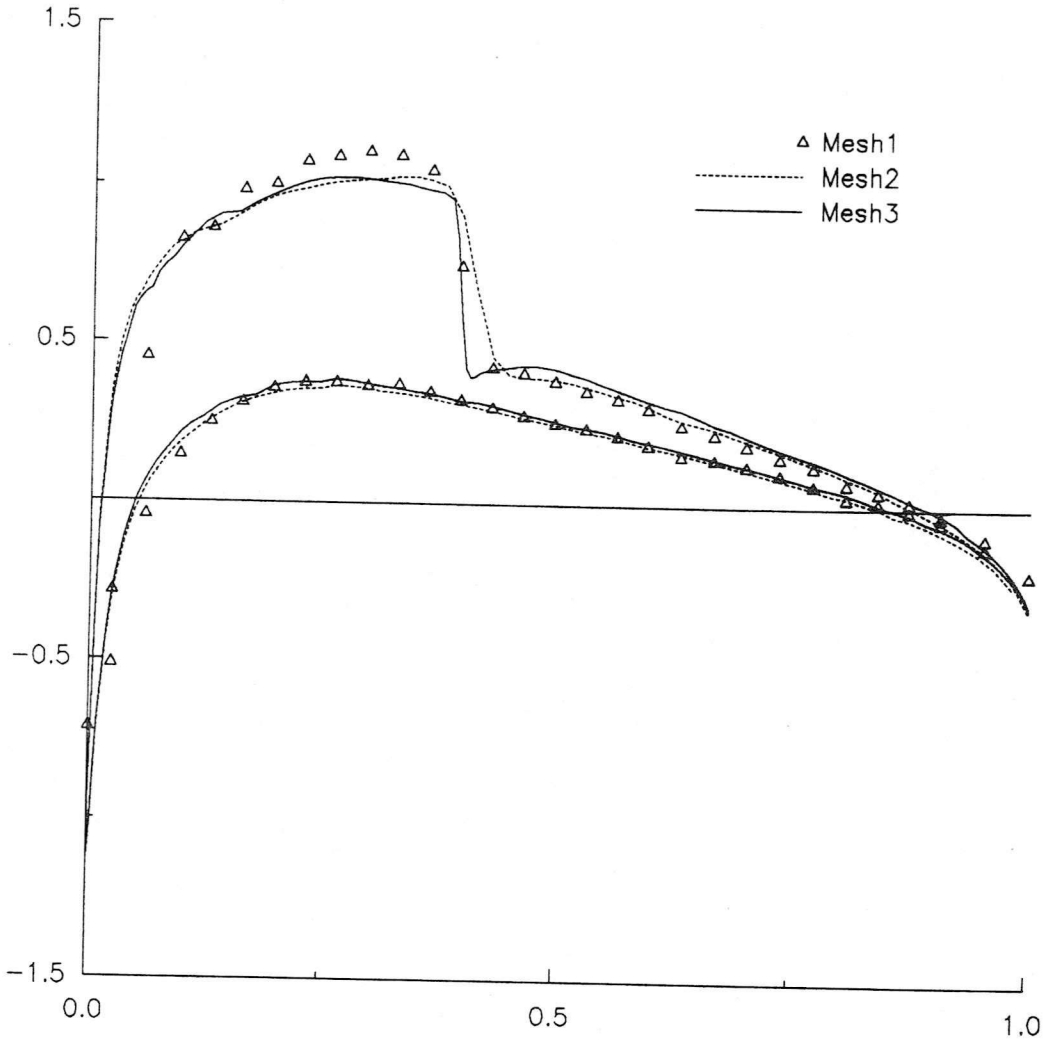

Figure 33 Comparison of Cp distributions on first, second and adaptive meshes
NACA 0012 Airfoil Mach=0.75 Alp=2.0 (Deg) first-order results

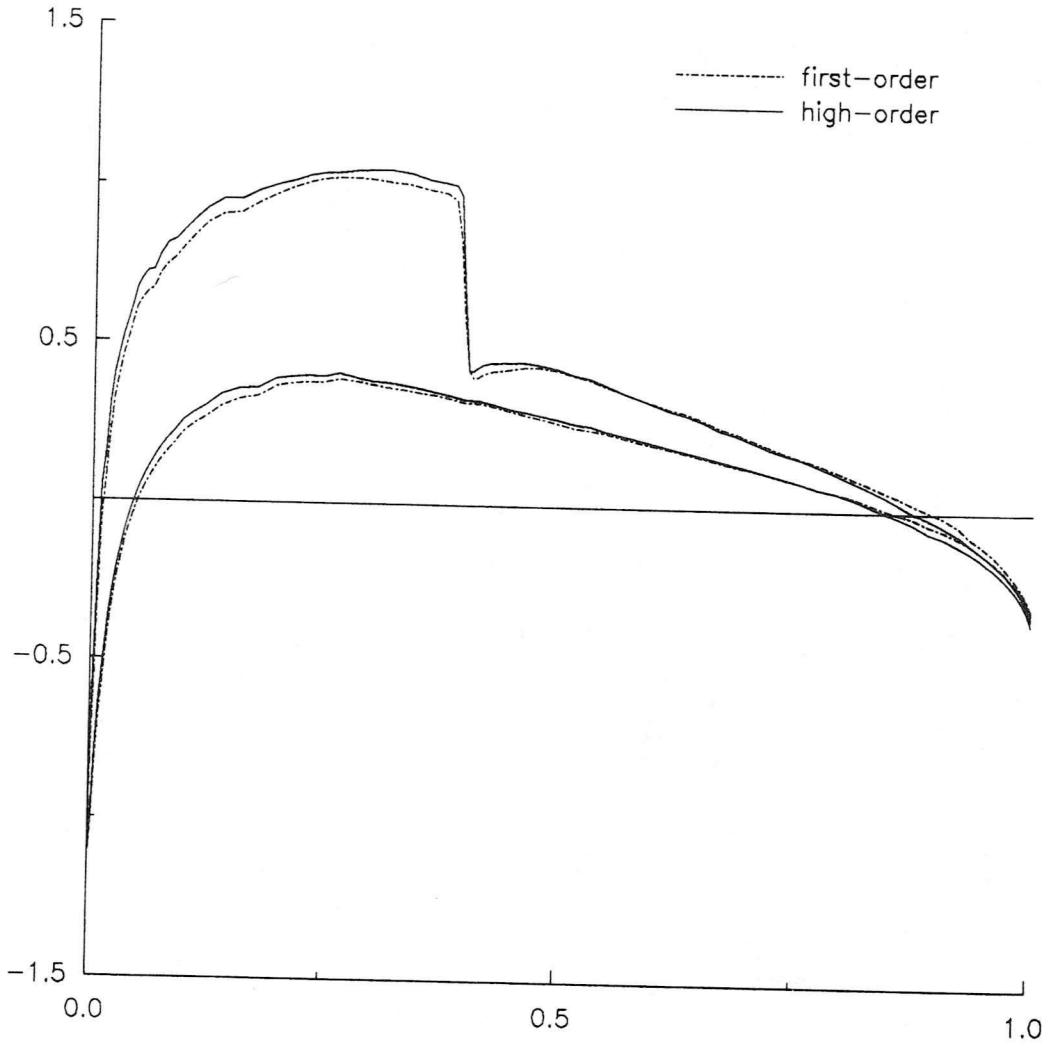

Figure 34 Comparison of Cp distributions of 1st order and 2nd order on adaptive mesh
NACA 0012 Airfoil Mach=0.75 Alp=2.0 (Deg)

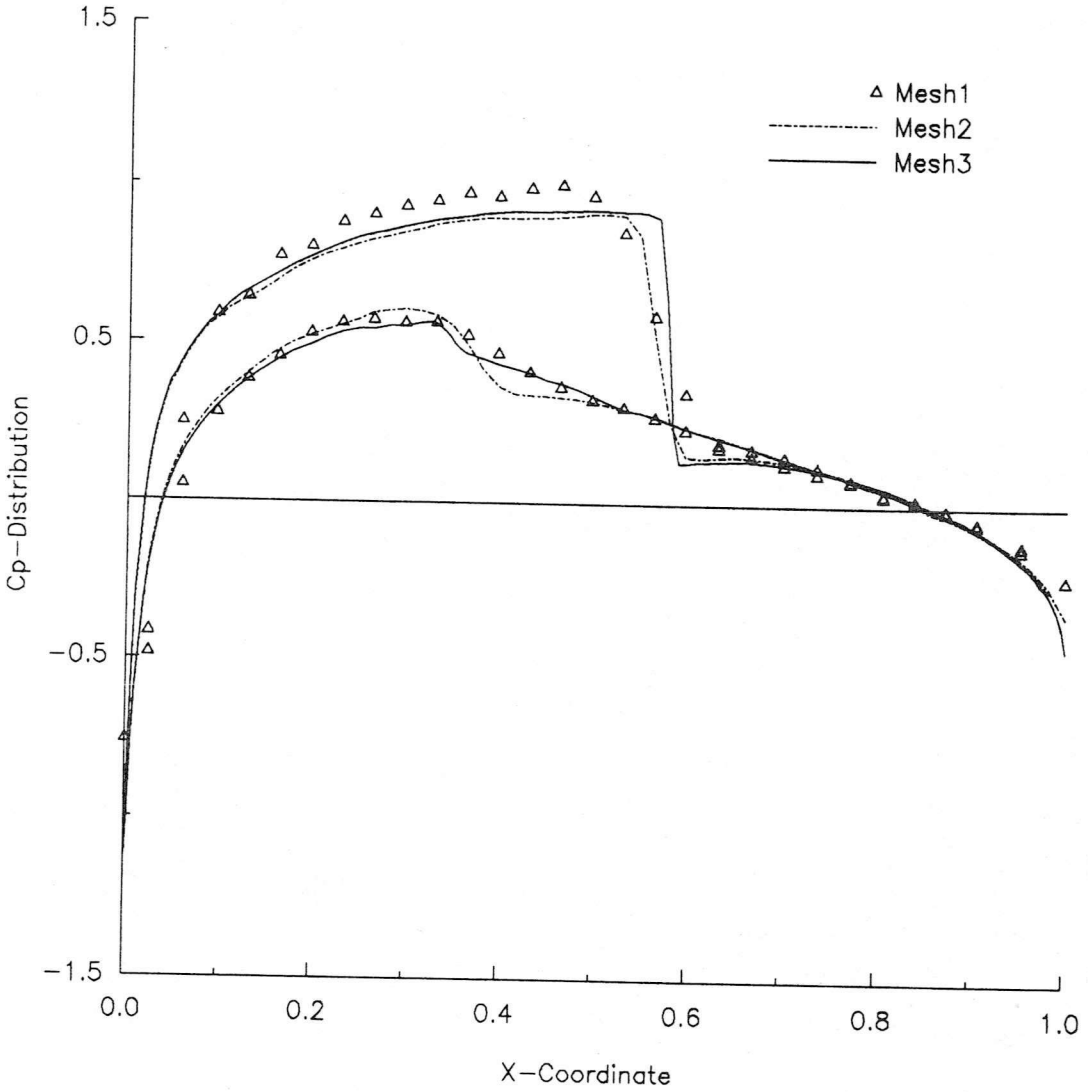

Figure 35 Comparison of Cp distributions on first, second and adaptive meshes
NACA 0012 Airfoil Mach=0.80 Alp=1.25 (Deg) first-order results

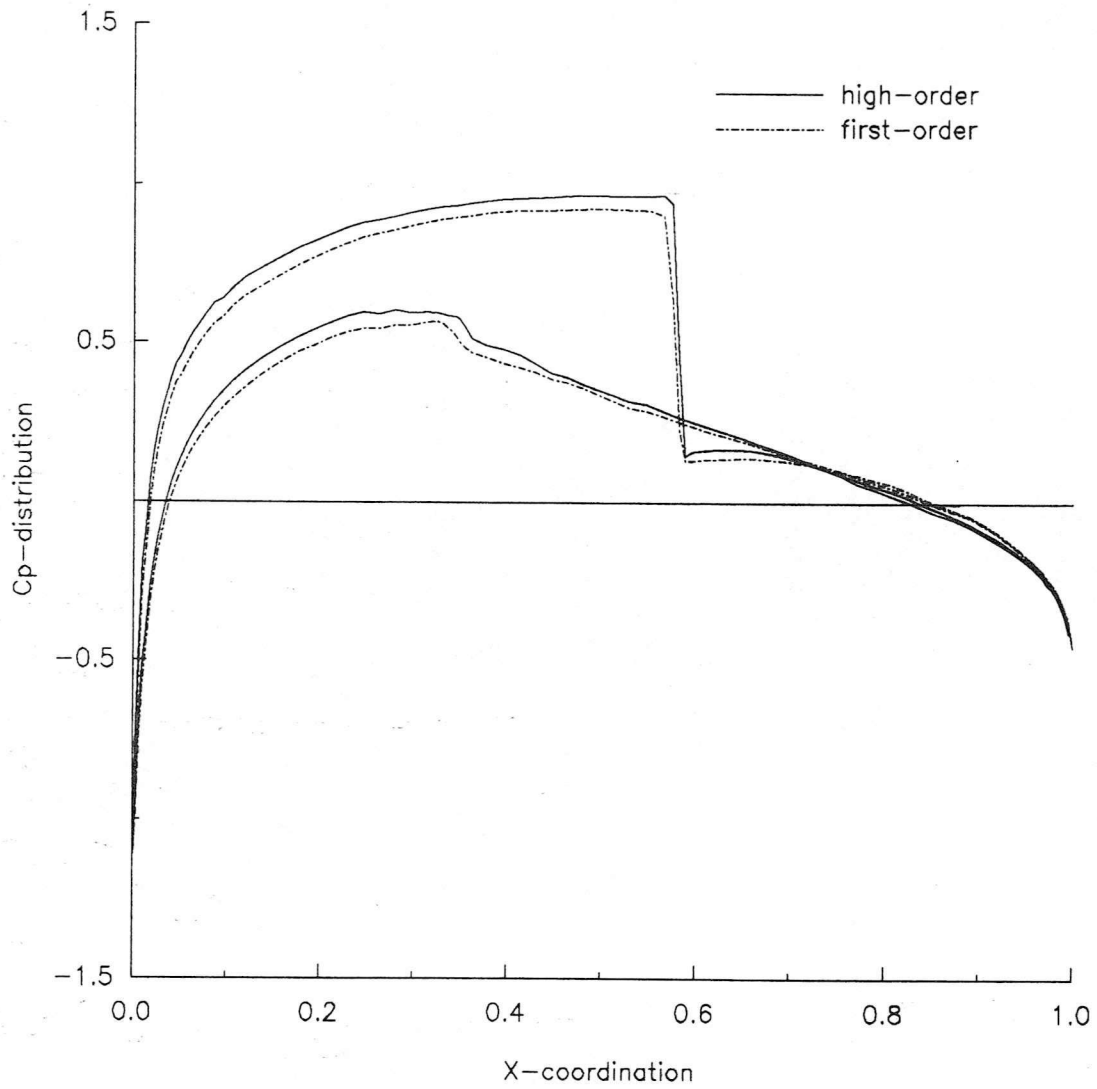

Figure 36 Comparison of Cp distributions of 1st order and 2nd order on adaptive mesh
NACA 0012 Airfoil Mach=0.80 Alp=1.25 (Deg)

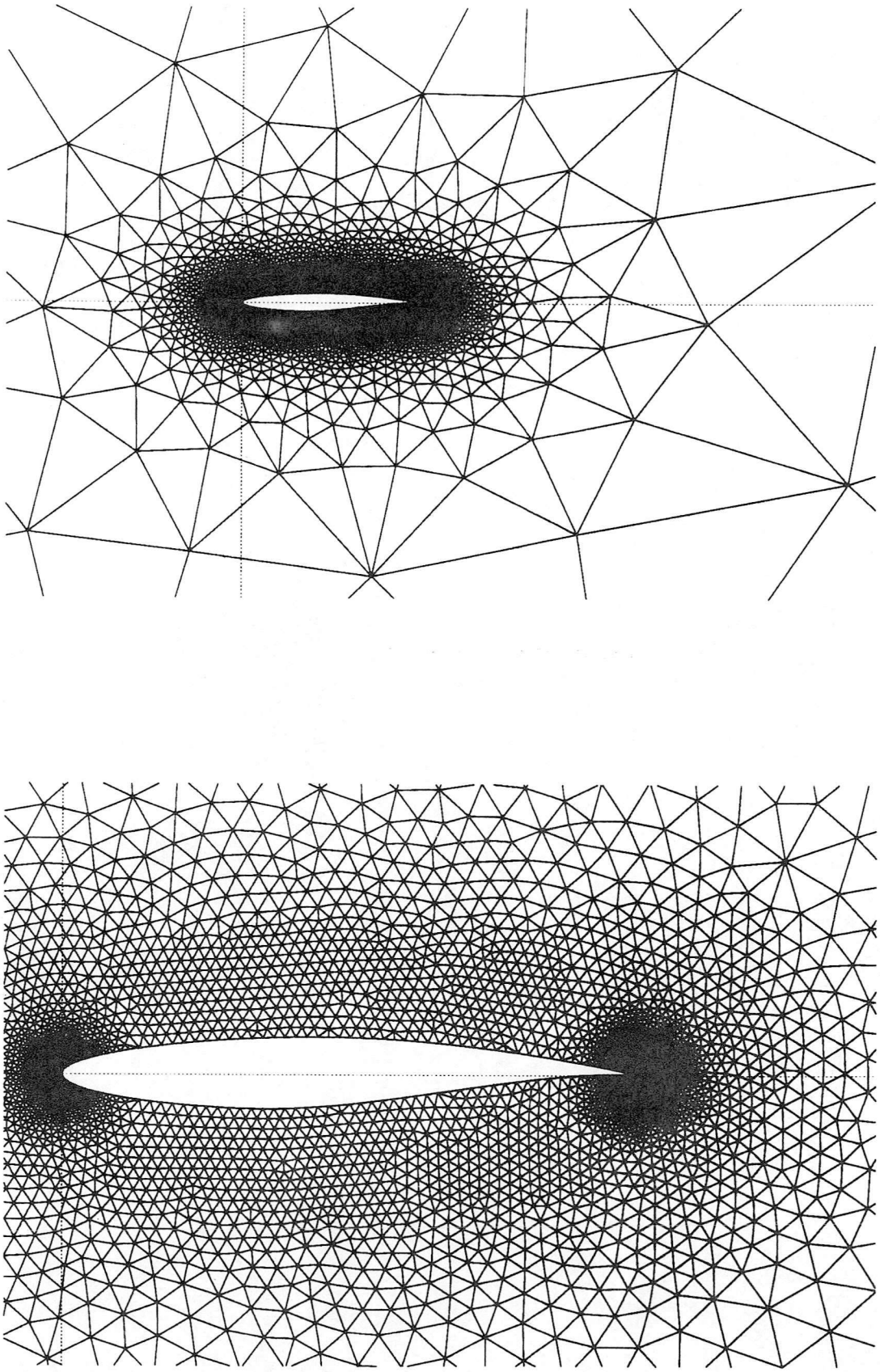

Figure 37 RAE 2822 Airfoil
Mesh 1 --- first triangulation of airfoil
6674 elements 3426 nodes

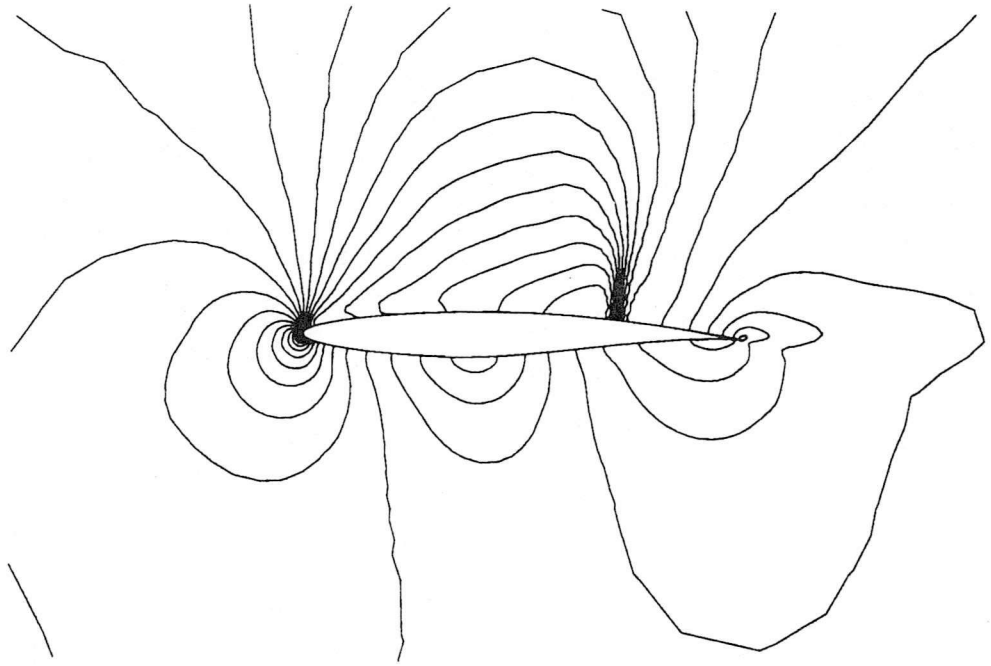

Figure 38(a) RAE 2822 Airfoil
Mach number contours on Mesh1
Mach=0.75 Alp=3.0 (Deg)

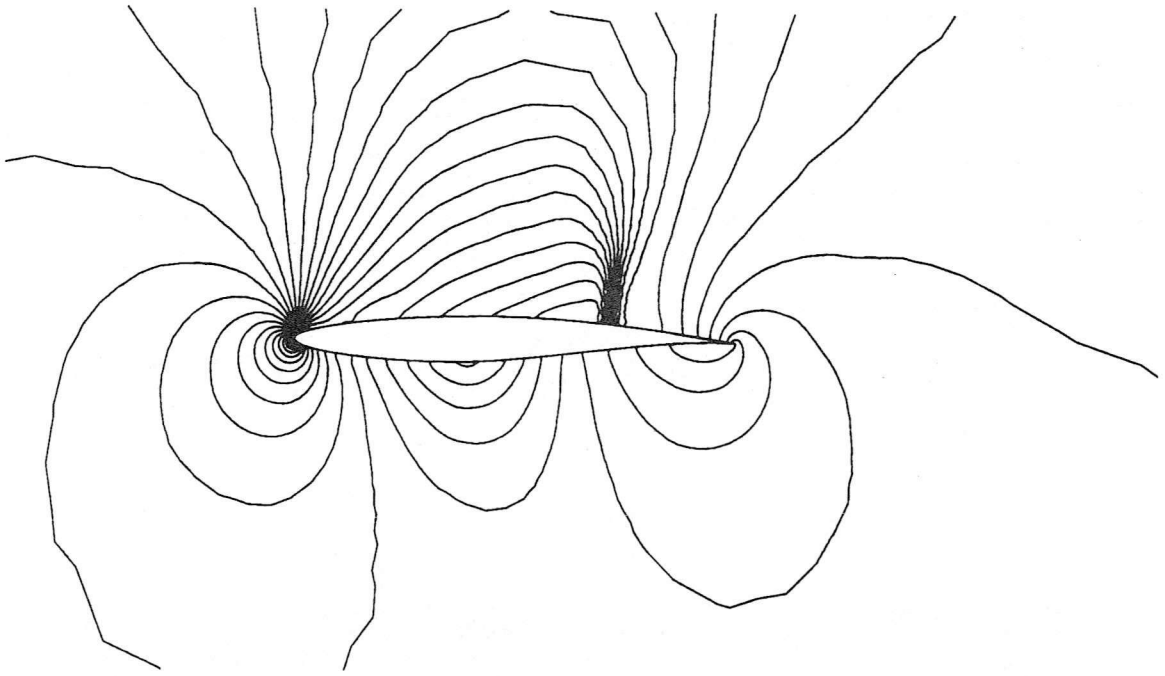

Figure 38(b) RAE 2822 Airfoil
Pressure contours on Mesh1
Mach=0.75 Alp=3.0 (Deg)

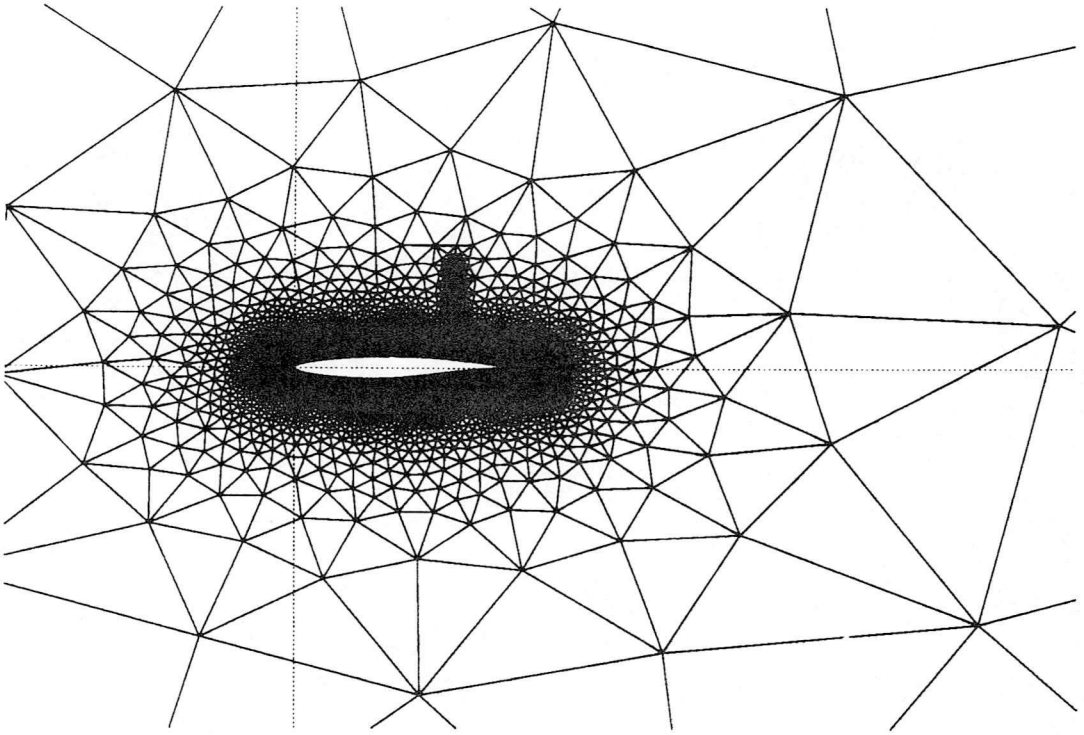

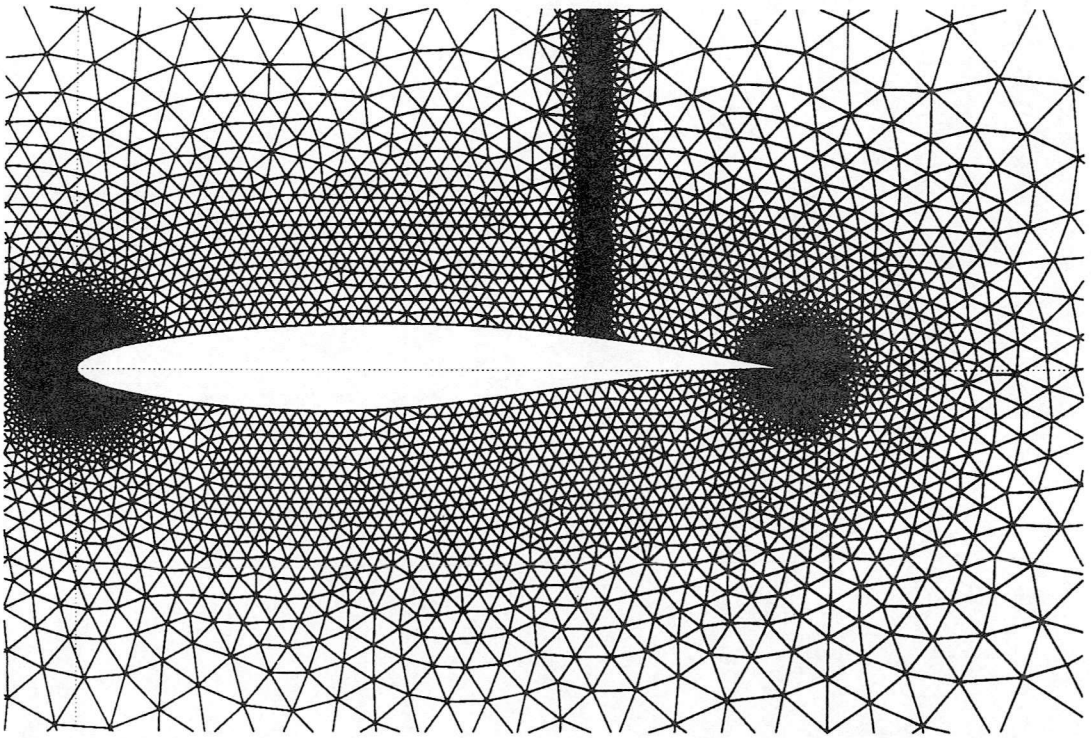

Figure 39 RAE 2822 Airfoil
Mesh 2 --- adaptive triangulation of airfoil on case (Mach=0.75 Alp=3.0)
9506 elements 4850 nodes

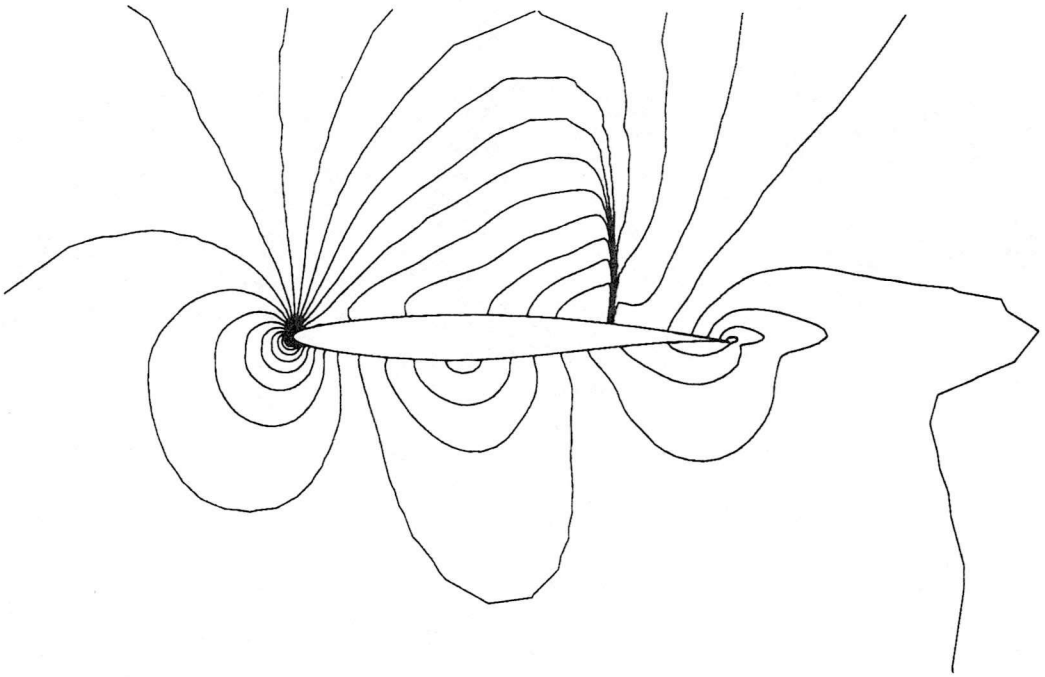

Figure 40(a) RAE 2822 Airfoil
Mach number contours on Mesh2
Mach=0.75 Alp=3.0 (Deg)
first-order results

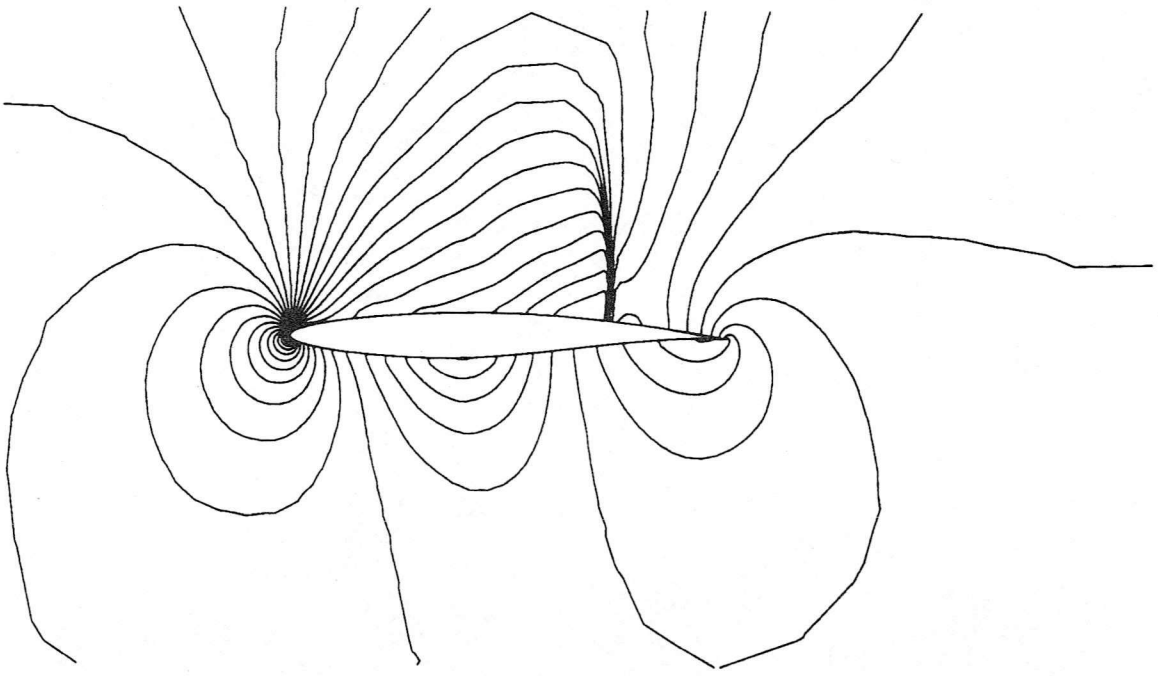

Figure 40(b) RAE 2822 Airfoil
Pressure contours on Mesh2
Mach=0.75 Alp=3.0 (Deg)
first-order results

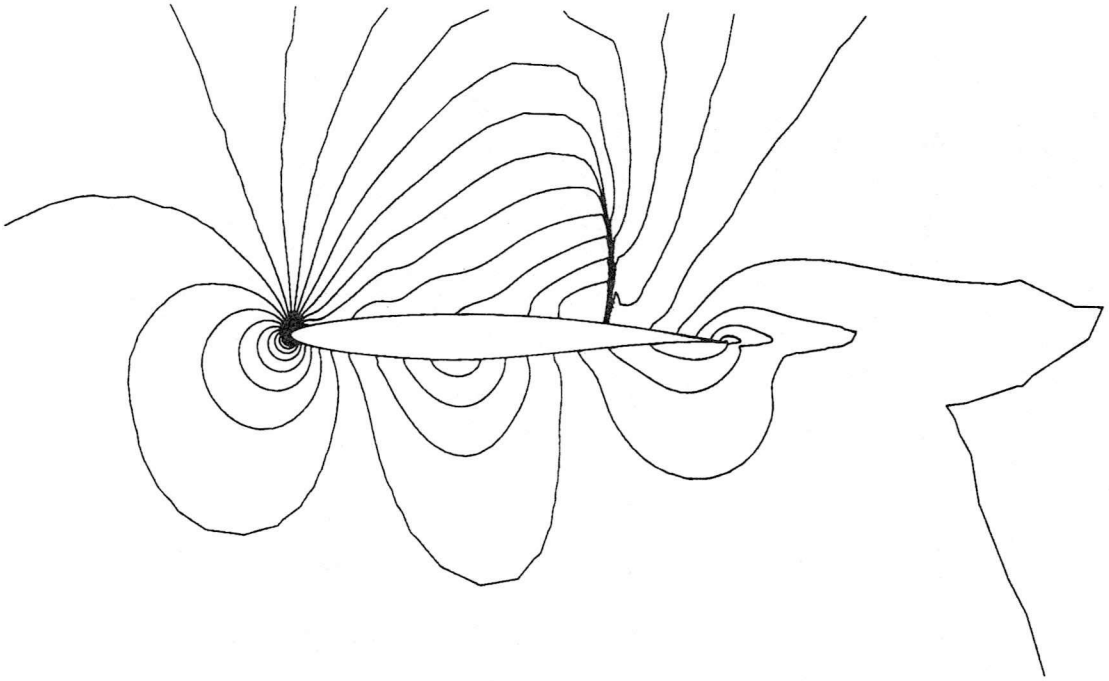

Figure 41(a) RAE 2822 Airfoil
Mach number contours on Mesh2
Mach=0.75 Alp=3.0 (Deg)
second-order results

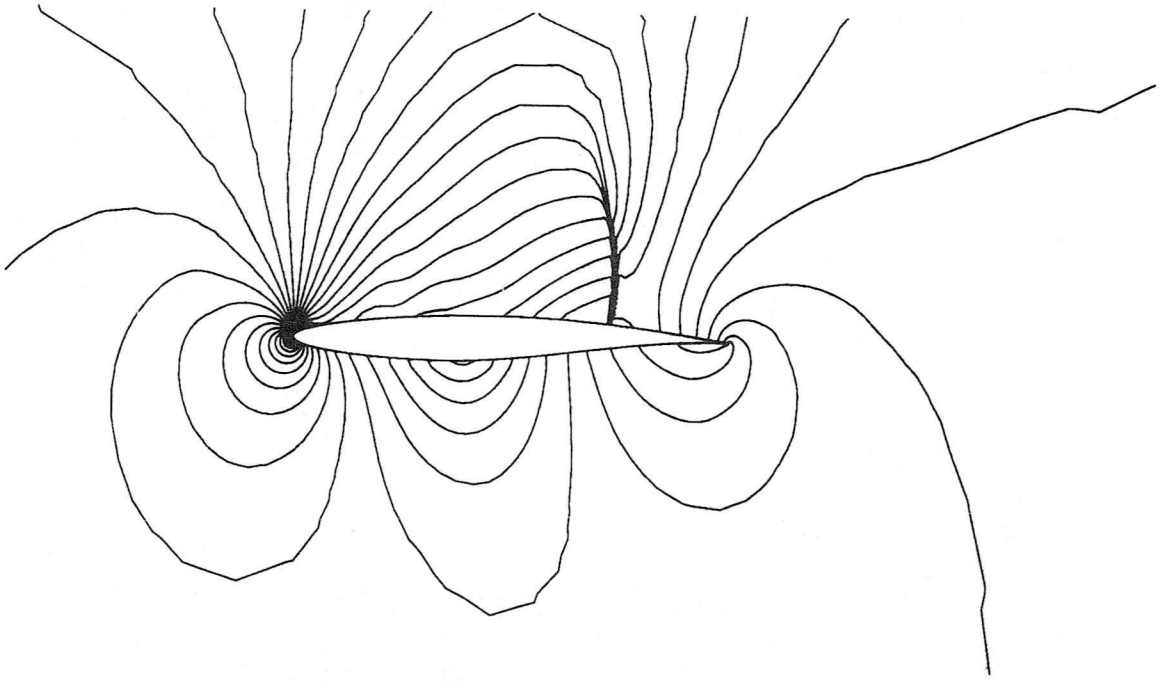

Figure 41(b) RAE 2822 Airfoil
Pressure contours on Mesh2
Mach=0.75 Alp=3.0 (Deg)
second-order results

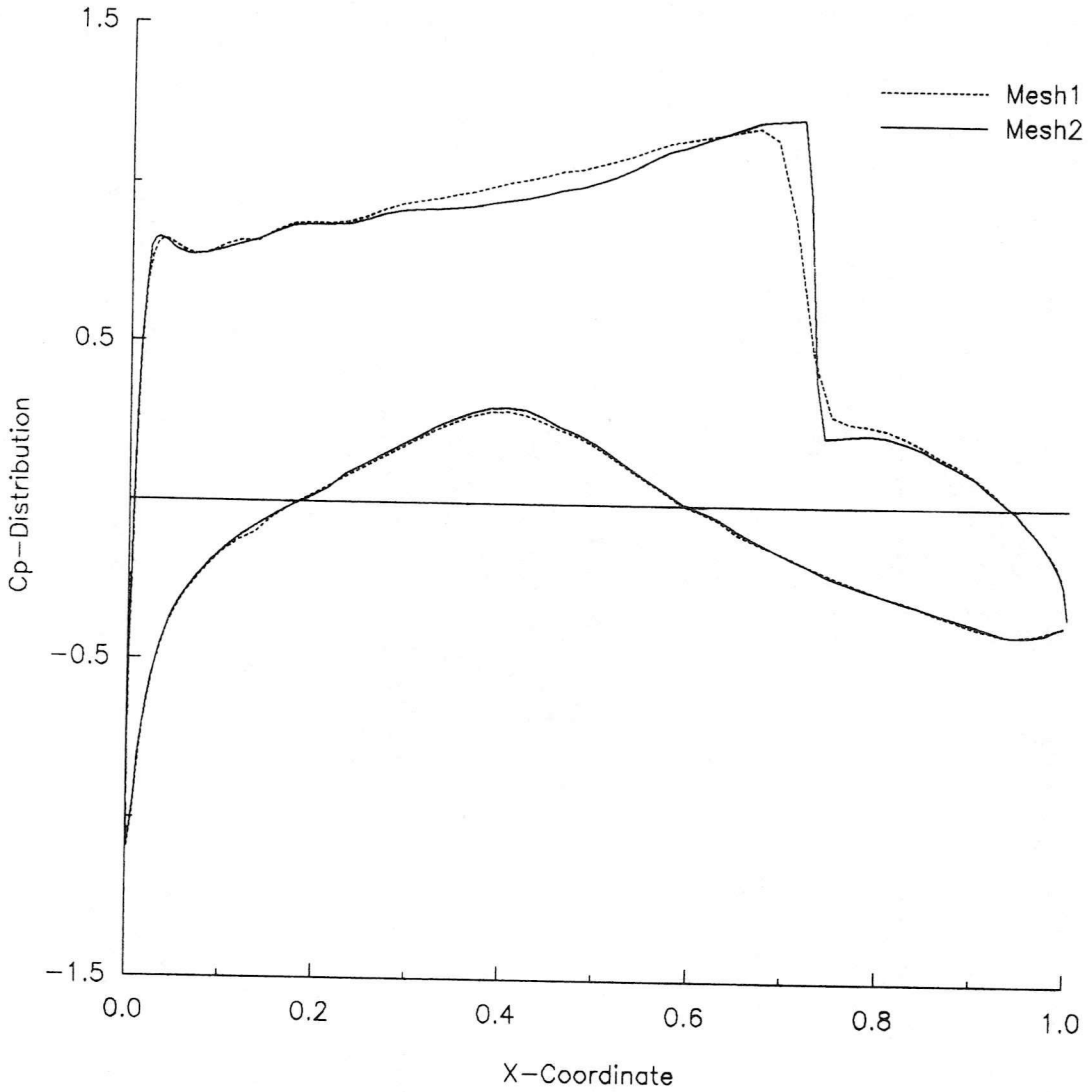

Figure 42 Comparison of Cp distributions on first and adaptive meshes
RAE 2822 Airfoil Mach=0.75 Alp=3.0 (Deg) first-order results

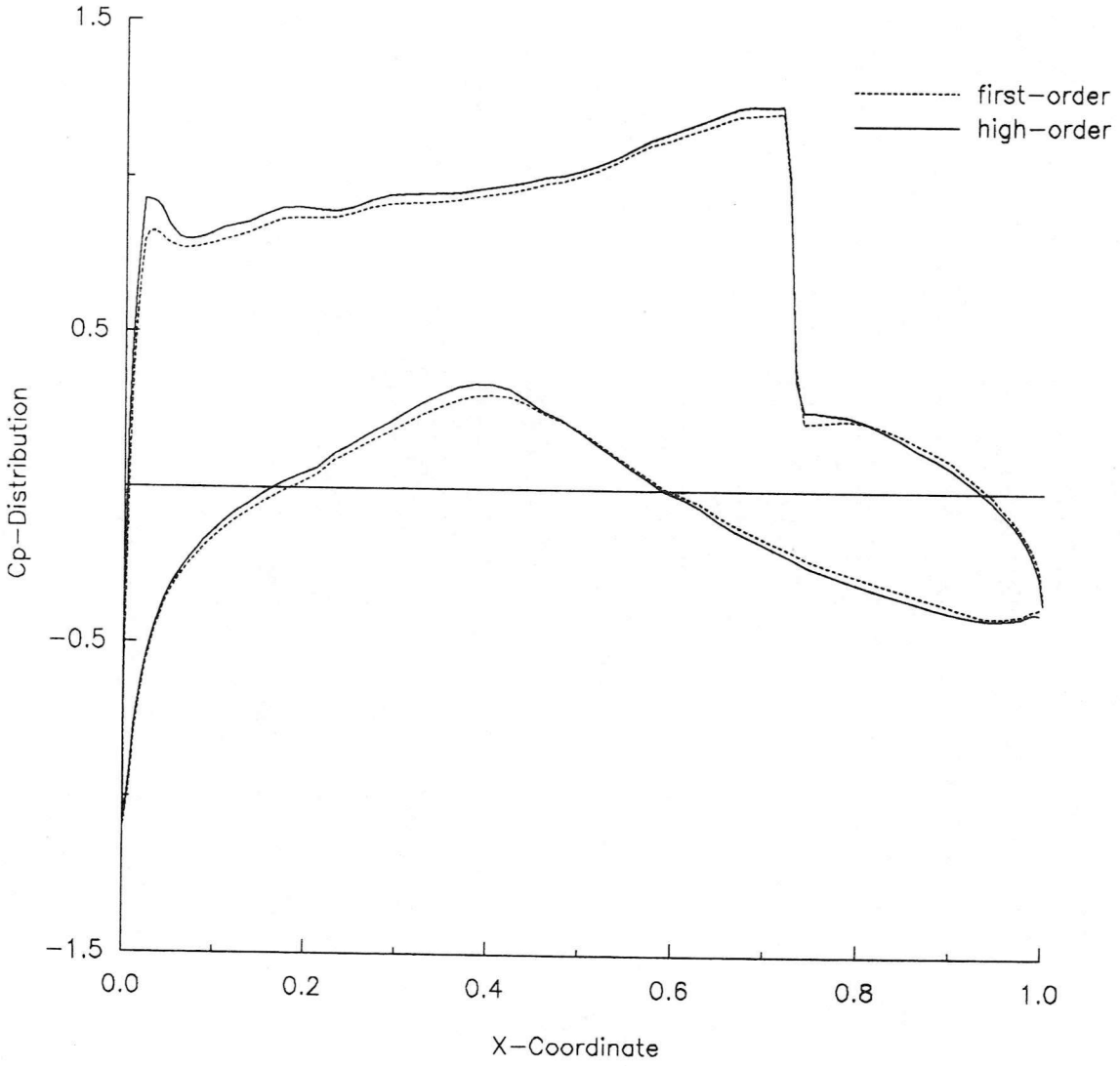

Figure 43 Comparison of Cp distributions of 1st order and 2nd order on adaptive mesh
RAE 2822 Airfoil Mach=0.75 Alp=3.0 (Deg)

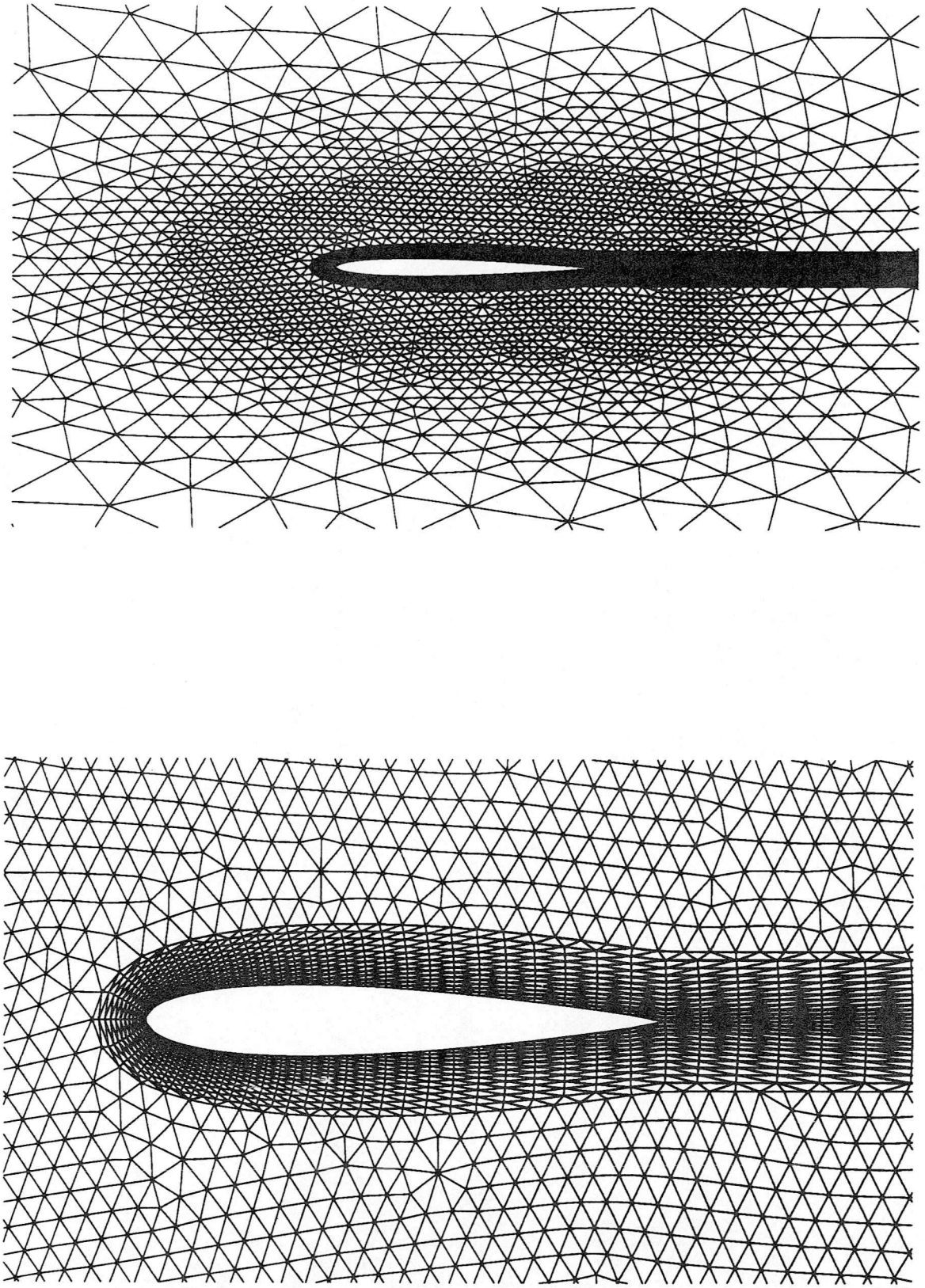

Figure 44 NACA 0012 Airfoil Combined-mesh
inner region : regular unstructured mesh
outer region : unstructured mesh

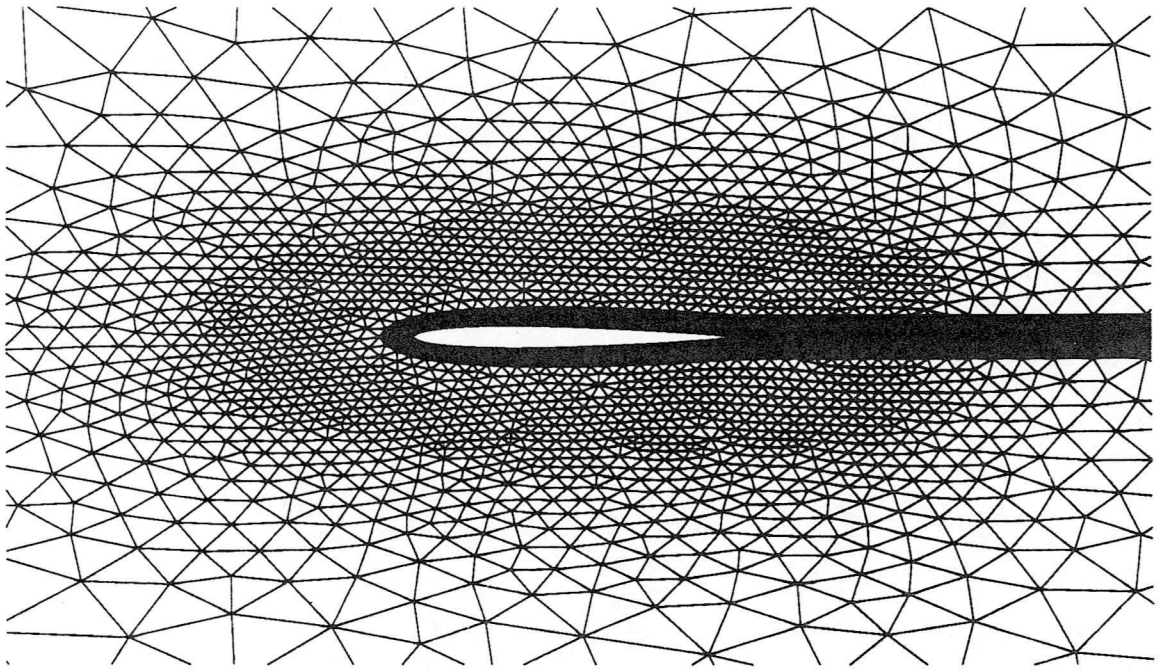

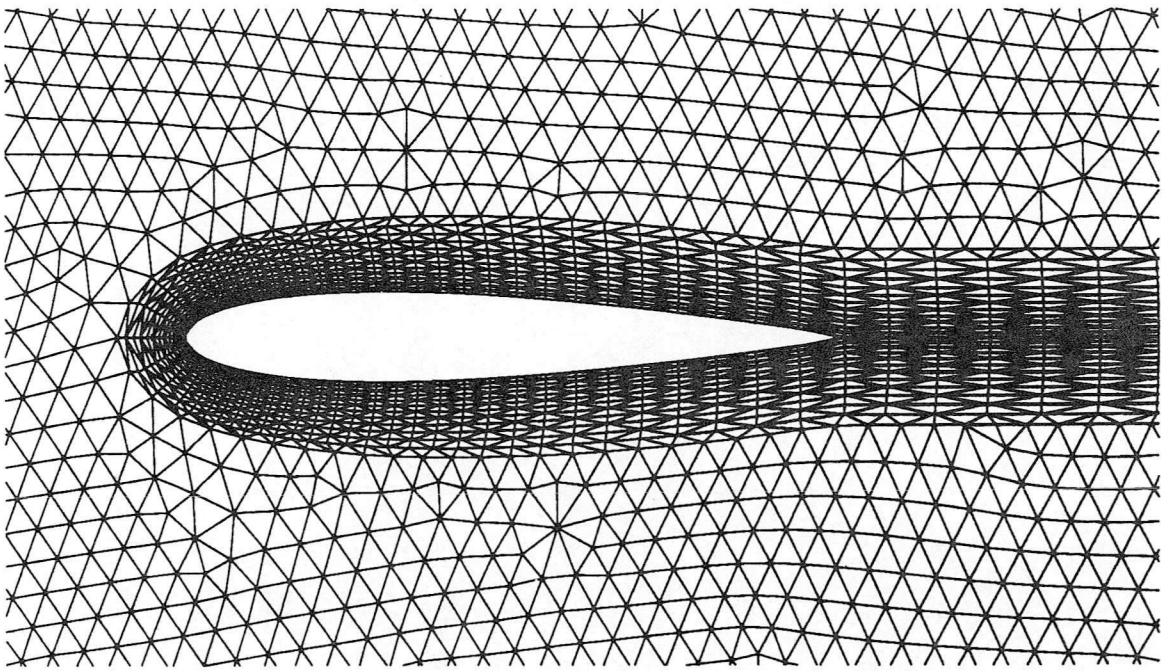

Figure 45 NACA 0012 Airfoil Combined-mesh
inner region : regular-stagged unstructured mesh
outer region : unstructured mesh

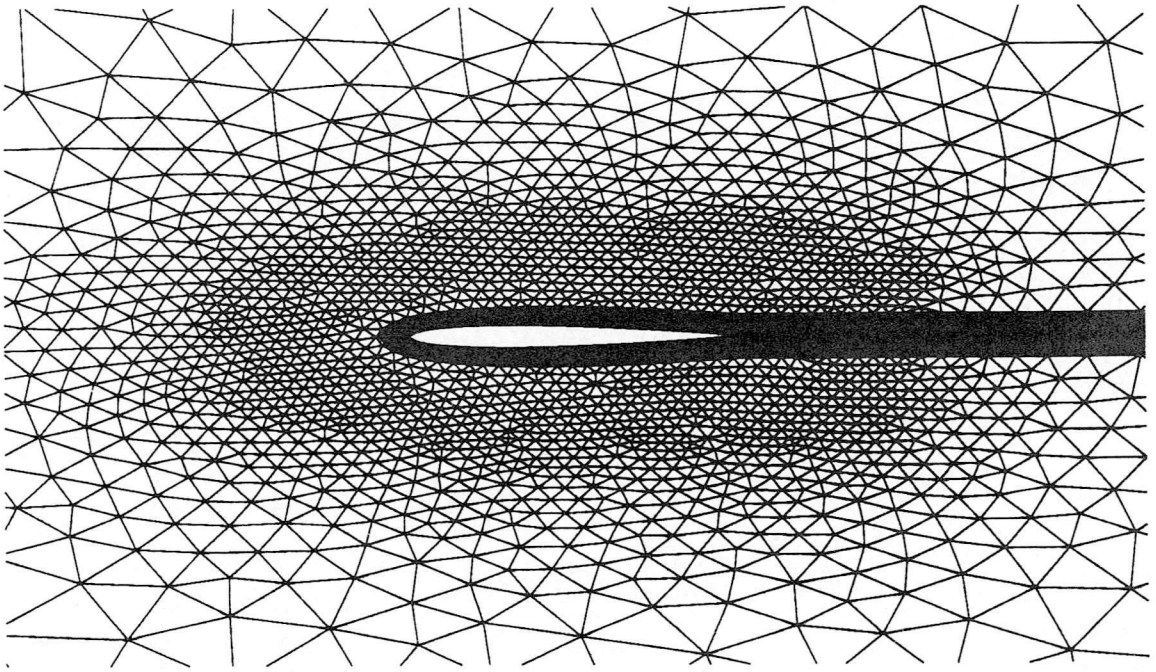

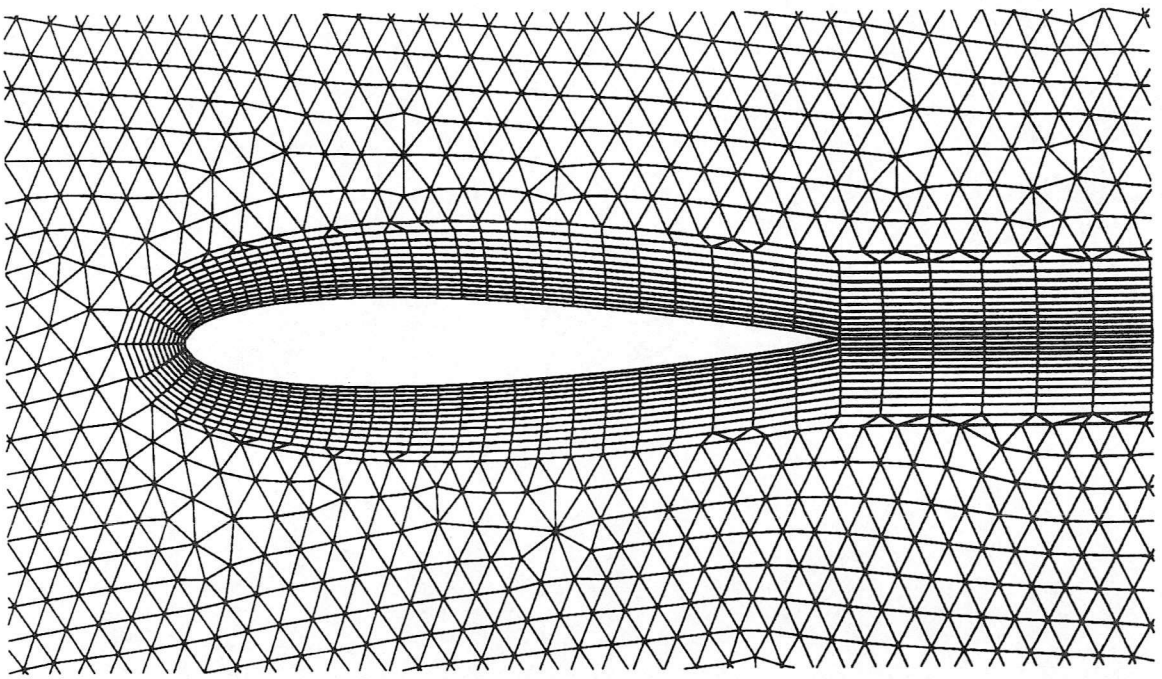

Figure 46 NACA 0012 Airfoil Hybrid-mesh
inner region : structured mesh
outer region : unstructured mesh